

Effects of three-dimensional crustal structure and smoothing constraint on earthquake slip inversions: case study of the Mw6.3 2009 L'Aquila earthquake

František Gallovič¹, Walter Imperatori^{2*}, P. Martin Mai²

¹ Charles University in Prague, Faculty of Mathematics and Physics, Department of Geophysics, Prague, Czech Republic (corresponding author, gallovic@karel.troja.mff.cuni.cz)

² King Abdullah University of Science and Technology (KAUST), Thuwal, Kingdom of Saudi Arabia

* Now at the Swiss Seismological Service (SED), Swiss Federal Institute of Technology ETH, Zurich

Abstract

Earthquake slip inversions aiming to retrieve kinematic rupture characteristics typically assume 1D velocity models and a flat Earth surface. However, heterogeneous nature of the crust and presence of rough topography lead to seismic scattering and other wave propagation phenomena, introducing complex 3D effects on ground motions. Here we investigate how the use of imprecise Green's functions – achieved by including 3D velocity perturbations and topography – affect slip-inversion results. We create sets of synthetic seismograms, including 3D heterogeneous Earth structure and topography, and then invert these synthetics using Green's functions computed for a horizontally layered 1D Earth model. We apply a linear inversion, regularized by smoothing and positivity constraint, and examine in detail how smoothing effects perturb the solution. Among others, our tests and resolution analyses demonstrate how imprecise Green's functions introduce artificial slip-rate multiples especially at shallow depths and that the timing of the peak slip-rate is hardly affected by the chosen smoothing. The investigation is extended to recordings of the 2009 Mw 6.3 L'Aquila earthquake, considering both strong motion and high-rate GPS stations. We interpret the inversion results taking into account the lessons learned from the synthetic tests. The retrieved slip model resembles previously published solutions using geodetic data, showing a large-slip asperity south-east of the hypocenter. In agreement with other studies, we find evidence for fast but sub-shear rupture propagation in up-dip direction, followed by a delayed propagation along strike. We conjecture that rupture was partially inhibited by a deep localized velocity-strengthening patch that subsequently experienced afterslip.

1. Introduction

On April 6th, 2009, the Abruzzo region in the central Apennines (Italy) was struck by an Mw6.3 earthquake, producing significant damage in the city of L'Aquila and its neighboring villages (Ameri et al., 2009). The event originated at 9km depth and ruptured a NE-SW-striking SE-dipping fault that is well-constrained by relocated aftershocks (Valoroso et al., 2013). The fault orientation and the normal-faulting mechanism are in agreement with the extensional trend of the central Apennines.

The L'Aquila earthquake has been studied extensively in terms of ground-shaking and earthquake source characterization, making use of the large amount of available high-quality data. Several studies have been devoted to slip inversions, using strong-motion stations (Poïata et al., 2012), static geodetic GPS and/or SAR data (Cheloni et al., 2010; Trasatti et al., 2011; D'Agostino et al., 2012; Serpelloni et al., 2012; Gualandi et al., 2014) including waveforms inferred from HR-GPS receivers (Avallone et al., 2011), and various data combinations (Cirella et al., 2009 and 2012; Zhang et al., 2012). Most of the studies reveal a complicated rupture evolution in which the co-seismic rupture initiated with fast up-dip (in-plane) rupture propagation (Tinti et al., 2014), followed by along-strike (anti-plane) delayed rupture propagation along a large-slip asperity. Based on geodetic data, significant afterslip has been inferred in areas of small co-seismic slip (Cheloni et al., 2010; D'Agostino et al., 2012; Yano et al., 2014). Gualandi et al. (2014) suggest that the region of postseismic slip does not migrate along the fault, and thus could be explained by stationary geologic conditions that lead to mildly velocity strengthening behavior.

Gallovič and Zahradník (2012) utilized near-source strong-motion data ($R < 50$ km) with maximum frequency of 0.2Hz to invert for a low-resolution representation of the rupture process, fitting the data satisfactorily with three homogeneous slip-patches. In the present study, we extend this earlier work by increasing the frequency range to 0.5Hz, considering only the closest stations (up to 20 km fault distance), but without sacrificing the azimuthal coverage. In addition, we include HR-GPS displacement records to augment the data set. We apply a linear slip inversion technique, and study the effects of using imperfect Earth crust models for computing the Green's functions. In addition, we analyze potential biases and artifacts due to applied smoothing constraint. To this end, we perform a series of synthetic tests to understand the behavior of our inversion scheme, which enables us to more reliably interpret the estimated kinematic rupture evolution. The main question we address here is: are we able to extract more information about the rupture process when limiting the inversion to data analyzed at short distances but higher frequencies, while using a more general source description?

Linear inversions with minimal a priori constraints, especially when using long time windows such as in the present paper, provide a general description of the source model. The result of the inversion is the estimation of the temporal evolution of slip-rate as a function of fault position without any prescribed nucleation point, shape of the slip-rate function, or rupture speed. Therefore, such a linear inversion has the potential to infer even very complex features of the rupture evolution, such as delays, slip reactivation (multiple rupturing), or rupture-propagation reversals. In principle, the formulation allows also to correctly reveal the supershear rupture propagation, together with the associated trailing Rayleigh pulse (Dunham and Archuleta, 2004; Mello et al., 2014).

Kinematic finite-fault earthquake source inversions constitute a non-unique inverse problem, which is often linearized by imposing strong a priori constraints (e.g., constant rupture velocity). In contrast, many studies using nonlinear inversion techniques, applied to synthetic test cases, document the strength of these methods to accurately estimate the rupture

process (e.g., Shao and Ji, 2012; Konca et al., 2013; Razafindrakoto and Mai, 2014). For example, Shao and Ji (2012) have demonstrated for the SPICE source inversion validation BlindTest 1 that the nonlinear inversion performs well. However, such “positive” tests are typically performed under idealistic conditions (frequency range 0-2Hz, precise Green’s functions and fault location, perfect station coverage, etc.) that are far from real-data applications. In some cases the authors “simulate” the real conditions, e.g., by introducing imperfections in the Green’s functions (Graves and Wald, 2001; Ji et al., 2002; Piatanesi et al., 2007; Konca et al., 2013; Razafindrakoto and Mai, 2014), or by adding uncorrelated Gaussian noise to the ‘observed’ data (Cohee and Beroza, 1994; Sekiguchi et al., 2000; Shao and Ji, 2012; Bernauer et al., 2014).

Interestingly, the apparent quality of the inverted slip models, derived for synthetic test cases, is in contradiction to the large variability found in rupture models for a single earthquake, obtained by different authors using various inversion methods and/or datasets (see the SRCMOD database (Mai and Thingbaijam, 2014) for numerous cases). For example, Clévéde et al. (2004) compare models of the Izmit earthquake inverted by various authors applying different inversion techniques, some of them being characterized by rupture complexities, and some not. To understand the inversion performance properly, one needs to perform synthetic tests under conditions that are as realistic as possible.

In this paper, prior to the real data application, we perform a series of synthetic tests to understand the behavior of linear slip inversion when applying a long time window in which slip is allowed to occur on each point of the fault (i.e. the time window is chosen as long as the total rupture duration). The inversion is stabilized by enforcing slip rate positivity and applying smoothing using an a priori defined covariance matrix. We then discuss in detail the effect of smoothing and the use of imperfect Green’s functions. All tests are performed under realistic conditions by considering i) real station distribution, ii) the same frequency range as used in the real data case, iii) the crustal model being based on 3D tomography and including topography and realistic random velocity variations. In the inversion tests we consider a smooth target model as well as a spike dislocation model to analyze the inversion resolution in detail. The Appendix discusses results for an additional synthetic test based on SIV1 benchmark. We then invert real data recorded during the Mw6.3 2009 L’Aquila earthquake using Green’s function calculated for a 3D tomographic model. We emphasize that the inversion result have to be interpreted carefully and case-dependent, taking into account the lessons learned from the synthetic tests, in order to be able to reliably conclude which of the model features are well resolved and which of them are questionable.

2. Inversion method

We consider a rectangular fault with length L and width W . The displacement wavefield $\mathbf{u}(\mathbf{r}, t)$ measured at station \mathbf{r} is related to slip rate $\Delta\dot{\mathbf{u}}(\boldsymbol{\xi}, t)$ distributed along fault $\Sigma(\boldsymbol{\xi})$ by means of representation theorem (Aki and Richards, 2002). Assuming that the earthquake slip direction is independent of time, the representation theorem simplifies to

$$\mathbf{u}(\mathbf{r}, t) = \iint_{\Sigma} \Delta\dot{\mathbf{u}}(\boldsymbol{\xi}, \tau) \mathbf{G}(\mathbf{r}, \boldsymbol{\xi}, t - \tau) d\boldsymbol{\xi} d\tau, \quad (1)$$

where $\mathbf{G}(\mathbf{r}, \boldsymbol{\xi}, t)$ is the displacement response of the medium at location \mathbf{r} due to a point excitation by a double-couple source at position $\boldsymbol{\xi}$ with unit step function in time (in the following we call \mathbf{G} as Green’s functions despite the more general definition by Aki and Richards, 2002).

Depending on how the slip rate functions are parameterized, two general classes of methods can be distinguished. The first class, linear inversion techniques (also called multi-time window) are based on a discretized version of the representation theorem (1). The slip rate functions are parameterized by elementary functions (overlapping narrow triangles, delta-like, etc.), acting in several time windows. The windows span various time intervals ranging from relatively small fraction of source duration (e.g., Hartzell and Heaton, 1983; Delouis et al., 2002) up to the total rupture duration (e.g., Olson and Anderson, 1988; Frankel and Wennerberg, 1989; Das and Kostrov, 1994; Gallovič et al., 2009; Gallovič and Zahradník, 2011, Fan et al., 2014). This formulation typically requires a large number of model parameters that are linearly related to the wavefield. The inversion is then performed considering regularization by applying smoothing and a positivity constraint. The second class of inversion methods, so called nonlinear (or parametric) inversion, utilizes the representation theorem as well, but the shape of the slip-rate function is prescribed a-priori. In this case, the source model is parameterized in terms of physical quantities (such as rupture-onset time, rise time, peak slip rate) that are, generally, nonlinearly related to the wavefield. Various non-linear optimization techniques have been applied to obtain earthquake rupture models that fit the utilized data (e.g. Hartzell and Liu, 1995; Hartzell et al, 1996; Piatanesi et al., 2007; Monelli and Mai, 2008)

The major advantage of nonlinear inversions is that they work with much lower number of parameters, thus allowing for an efficient uncertainty analysis (Monelli et al., 2009; Cirella et al., 2012; Gallovič and Zahradník, 2012; Razafindrakoto and Mai, 2014). In contrast, although the linear inversion can now be performed fast and efficiently on common desktop computers, any practical uncertainty analysis is prohibited due to the overwhelming number (thousands) of model parameters. Thus, these methods can be tested only by synthetic tests, such as those performed in the present paper.

Our method is based on a linear approach, in which the spatial and temporal integrals in (1) are discretized with steps ΔL , ΔW , Δt , respectively. The representation theorem (1) can then be expressed in matrix form as $\mathbf{d}=\mathbf{G}\mathbf{m}$, where vector \mathbf{d} contains the displacement wavefield \mathbf{u} of all stations and components considered, vector \mathbf{m} encompasses model parameters in terms of spatial and temporal samples of the slip rate. Alternatively, one can think of the model parameterization as by means of a piecewise constant function in time and space, where model parameters \mathbf{m} consists of its space-time amplitudes. Matrix \mathbf{G} contains the responses to point-source excitations by the individual elementary spatial-temporal elementary subfaults of model vector \mathbf{m} .

Our inverse problem requires regularization. We assume that, statistically, the model parameters are close to prior model \mathbf{m}_A with prior covariance matrix \mathbf{C}_M (acting as a smoothing constraint). Furthermore, we apply a weighted constraint on the value of the slip model's seismic moment, assuming that it is equal to a previously determined value M_0 . Thus, we aim at minimizing the L2-norm misfit function (here shown in non-dimensional form),

$$M(\mathbf{m}) = \frac{1}{2}(\mathbf{d} - \mathbf{G}\mathbf{m})^T \mathbf{C}_D^{-1}(\mathbf{d} - \mathbf{G}\mathbf{m}) + \frac{1}{2}(\mathbf{m} - \mathbf{m}_A)^T \mathbf{C}_M^{-1}(\mathbf{m} - \mathbf{m}_A) + \frac{1}{2\sigma_{M_0}^2}(\mathbf{E} \cdot \mathbf{m} - M_0)^2, (2)$$

where \mathbf{C}_D denotes the data covariance matrix, σ_{M_0} is the weight of the seismic moment constraint, and \mathbf{E} is a vector of seismic moments of the elementary subfaults, $E_i = \mu_i \Delta L \Delta W \Delta t$. We assume $\sigma_{M_0} = M_0$ and $\mathbf{m}_A = 0$. We consider \mathbf{C}_M to be composed of discretized covariance function $\sigma_M^2 c_M(\tau, x, y)$ with temporal lag τ , and with spatial lags x (along strike) a y (along dip), where σ_M is the marginal standard deviation of the model parameters (c_M itself has unit

variance). We assume further that the Fourier spectrum of c_M (i.e. slip-rate power spectral density) is proportional to

$$c_M(f, k_x, k_y) \sim \left(\frac{1}{1 + (k_x L)^2 + (k_y W)^2} \right)^2. \quad (3)$$

Therefore, prior model parameters are statistically independent of time, and in the spatial domain they follow k^{-2} amplitude spectrum (with radial wavenumber $= \sqrt{k_x^2 + k_y^2}$). The particular choice of the spectral decay in (3) follows theoretical (Andrews, 1980; Herrero and Bernard, 1994) and observational (Somerville et al., 1999; Mai and Beroza, 2002) studies on spatial properties of earthquake slip distributions.

We apply the non-negativity constraint on the slip rates by means of the Nonnegative Least-Squares (NNLS) method (Lawson and Hanson, 1974). In summary, we solve the following augmented system of equations corresponding to the problem (2),

$$\begin{pmatrix} \mathbf{U}_D^{-T} \mathbf{G} \\ \frac{1}{\sigma_M} \mathbf{U}_M^{-T} \\ \frac{1}{\sigma_{Mo}} \mathbf{E} \end{pmatrix} \mathbf{m} = \begin{pmatrix} \mathbf{U}_D^{-1} \mathbf{d} \\ \mathbf{0} \\ \frac{1}{\sigma_{Mo}} M_0 \end{pmatrix}. \quad (4)$$

In Equation (4), matrices \mathbf{U}_D and \mathbf{U}_M are (upper-)triangular matrices obtained by Cholesky decomposition ($\mathbf{C} = \mathbf{U}^T \mathbf{U}$) of \mathbf{C}_D and \mathbf{C}_M , respectively. The augmented matrix and augmented data vector in (4) are inputs to the NNLS subroutine by Luo and Duraiswami (2011) that takes advantage of the efficient multicore Intel MKL library. We note that Fan et al. (2014) formulated the linear inverse problem in frequency domain, which, however, prevented them from applying the positivity constraint.

For simplicity, we consider all data points statistically independent and identically distributed (i.i.d). For such a particular choice the data covariance matrix becomes $\mathbf{C}_D = \sigma_D \mathbf{I}$, where \mathbf{I} and σ_D are the identity matrix and the data standard deviation, respectively, and $\mathbf{U}^{-1} = \mathbf{U}^T = 1/\sigma_D \mathbf{I}$ in equation (4).

In the following, we test effects of the chosen smoothing constraint, controlled by the ratio of data and prior-model standard deviations, σ_D/σ_M . Therefore, without loss of generality we can fix, e.g., σ_M at a prescribed value (1m/s in the present application). Then the smoothing strength is controlled formally just by the value of σ_D . Note that σ_D represents the data error (in meters). Thus, if the data error is considered large (by setting σ_D large), the smoothing constraint dominates the result, and vice versa.

3. Data

Strong motion data of the L'Aquila earthquake were recorded by a dense network of near-field accelerometric stations. The closest recording sites lie above the causative fault: station AQQ is a part of an array deployed in the upper Aterno-river valley, and AQU is located in downtown L'Aquila. At epicentral distances up to ~20 km the earthquake was recorded by another five stations, namely GSA (Gran Sasso), MTR (Montereale), FMG (Fiamignano), ANT (Antrodoto), CLN (Celano). The AQU station belongs to the MedNet network (<http://mednet.rm.ingv.it/data.php>), while the remaining ones belong to the Italian strong-motion network (RAN) (<http://www.protezionecivile.gov.it/jcms/it/ran.wp>). In addition, the earthquake was recorded by two 10 Hz GPS receivers situated just above the causative fault (ROIO, Poggio di Roio, and CADO, Fossa), located at 2.3 km and 10.4 km epicentral distance, respectively. Figure 1 shows location of these stations along with the surface-projection of the assumed rupture plane.

The accelerometric records have been detrended and band-pass filtered using a causal (minimum-phase) 4th order Butterworth filter (corner frequencies 0.05Hz and 0.5Hz). The lower frequency is given by the presence of instrumental noise in the data, while the upper corner has been found as the maximum frequency at which we can reliably compute the Green's functions. Avallone et al. (2011) processed the raw 10Hz GPS data to obtain ground displacement records; resulting HR-GPS waveforms are low-pass filtered using a causal (minimum-phase) 4th order Butterworth filter with corner frequency at 0.5Hz. This processing removes effects of a ~1Hz harmonic wave observed at CADO, which has been interpreted as a waveguide effect (Avallone et al., 2014). For the synthetic experiments in this study we apply the same filter to both computed and real accelerometric and HR-GPS data to provide a consistent picture of the inversion performance.

4. Fault model and 3D Green's functions

We assume the same fault plane as used by Gallovič and Zahradník (2012) and Ameri et al. (2012). The parameters are listed in Table 1. The fault plane measures 20 km along strike and 15 km down-dip.

To examine how inaccurate Green's functions affect the source inversion, we consider three velocity models with different level of complexity (Figure 2). The first model (C1) is a 1D velocity model composed of homogeneous horizontal layers, as utilized by Ameri et al. (2012) and Gallovič and Zahradník (2012). Such flat-layered crustal models are commonly assumed in source inversion studies. The second crustal model (C2) is the 3D tomographic velocity model of Di Stefano et al. (2011), derived by inverting P- and S-wave travel times observed on a dense local network. Finally, we introduce a third model (C3) in which we add small-scale random velocity perturbations to the previous deterministic 3D model C2 following the work of Imperatori and Mai (2013). In particular, the random field is characterized by a Von Karman correlation function with correlation length of 5 km, Hurst exponent 0.3 and standard deviation 10%. Although there is ambiguity in the choice of the correlation function parameters, the values used in this study are commonly assumed for the upper crust (Hartzell et al., 2010, Imperatori and Mai, 2013; Takemura and Furumura, 2013). In addition, we introduce the topography of the area into models C2 and C3. To maintain similar fault depths across all models, we align the average elevation above sea level (675m) in models C2 and C3 with the surface of the flat model C1.

Velocity heterogeneity and topography are responsible for complex wave propagation phenomena such as scattering, multi-pathing and mode conversion (e.g., Lee et al., 2009; Imperatori and Mai, 2013). Recently, Magnoni et al. (2014) have shown that during the L'Aquila earthquake the topographic relief influenced ground motion already at low frequencies, especially the coda waves. Their study also pointed out that lateral heterogeneities were essential for reproducing many of the recorded waveform complexities.

In our study we use model C3 to compute synthetic seismograms that are then treated as input data for testing the inversion when assuming velocity models C1 or C3. Velocity model C2 is used later in the inversion of observed data of the L'Aquila event.

We recall that matrix \mathbf{G} of the forward problem (see Equation 4) contains displacement waveforms at elementary subfaults distributed along the fault. We compute the corresponding seismograms for each subfault-receiver pair up to maximum frequency of 0.5 Hz. Each subfault has the same fault mechanism (Table 1), a unit scalar seismic moment, and effectively impulse slip rate function (i.e. rise-time is shorter than the inverse of maximum frequency). In the remainder of this study, we refer to these waveforms as Green's functions.

Green's function calculations are carried out using the second-order finite-difference code WPP (Nilsson et al., 2007). The numerical method is based on summation-by-part stencils, featuring efficient absorbing boundaries, vertical mesh refinement and visco-elastic attenuation (Petersson and Sjögreen, 2012). In addition to heterogeneous Earth models, the code also handles complex topography by means of curvilinear grid meshing. To obtain 40 sec-long time-series, the computational time required for each simulation reaches up to 25 minutes on 2048 cores of a BlueGene-P if topography is included.

5. Inversion model setup

The fault plane discretization described above must be chosen such that the representation integral (Equation 1) is correctly evaluated up to the highest frequency of interest. In particular, the sub-fault size must be a fraction of the minimum wavelength in the modelling, given by the ratio between the maximum frequency and the minimum velocity in the model. Note that under-discretization of the fault (i.e. considering too large subfaults) leads to artificial ringing effect in the synthetics (e.g., Spudich and Archuleta, 1987; Sekiguchi et al., 2002; Beresnev, 2003).

Considering a maximum frequency of 0.5Hz, corresponding to a shortest resolved wavelength of ~6km, we find that a 1km discretization step, both along dip and along strike, is sufficient. The temporal sampling is set to 0.4s. Since the corresponding Nyquist frequency (1.25 Hz) is well above the maximum frequency considered, each slip-rate sample represents effectively a delta function (see Section 2).

The inversions are performed using three-component displacement waveforms. We define station weights to balance the importance of stations in the inversion (Table 1). In particular, we assign low weights to the high-rate GPS stations since they have relatively long duration (due to the static displacement), and apply high weights to the far-distant stations to compensate for their smaller amplitudes due to geometrical spreading. We do not show effects of station coverage throughout the paper because, with the chosen station weights, the effect of removing a single station is small, although selected station weights may have an effect on the bias of the estimated slip model; this will be discussed later in the text.

6. Synthetic tests

Let us first review some general properties of the linear slip inversion. Despite being not explicitly expressed in Equation (4), the minimization of misfit function (2) is implicitly controlled by the condition number of matrix $\mathbf{G}^T\mathbf{G}$. We note that matrix \mathbf{G} of the forward problem is composed of Green's functions (GFs), and thus $\mathbf{G}^T\mathbf{G}$ contains cross-correlations of the GFs along the fault. Therefore, the performance of linear slip inversion is determined by the variability of the GFs along the fault. Due to the necessity of fine fault sampling to accurately compute the representation integral, adjacent GFs are very similar, and hence strongly correlated. This effectively lowers the rank of $\mathbf{G}^T\mathbf{G}$, and thus this matrix is generally not invertible. To correct for this, regularization by smoothing or inclusion of a prior covariance matrix must be performed. In particular, in case of distant (near regional) receivers, the difference between neighboring GFs is merely a time shift, leading to strong spatial-temporal trade-offs (Zahradník and Gallovič, 2010; Gallovič and Zahradník, 2011). In the extreme case of using only direct S waves, modelled as rays in the Fraunhofer approximation, the forward problem becomes equivalent to the Radon transform with a well-

defined kernel in the space-time domain, implying that in principle some slip models cannot be inferred (e.g., Menke, 1985; Bindi and Caponnetto, 2001).

In the present applications, we deal with near source data in a 1D layered and 3D complex structures. Therefore, the wavefield is inherently complex, even at relatively low-frequencies ($< 0.5\text{Hz}$), comprising near-field and intermediate-field terms (consisting of both P and S waves) and free surface effects. Therefore, the GFs are much more variable along the fault plane with respect to the near-regional case, and thus $\mathbf{G}^T\mathbf{G}$ is better conditioned, and the inversion should be better constrained. Nevertheless, we stress that it is important to first properly understand the effects of smoothing and utilization of imperfect GFs before application to the real data.

As an initial test (target) model we assume a simple Haskell-like slip distribution (Figure 3), resolved onto the fault plane of the L'Aquila earthquake. Slip is constant along dip, while in the along-strike direction it is characterized by smoothly varying amplitude with two distant maxima. The rupture propagates radially from the hypocenter, chosen as the actual hypocenter of the L'Aquila earthquake (Table 1). The shape of the target slip rate functions and its rise time are constant along the fault. The rupture-front arrival in the bottom-right of the fault is chosen to be delayed by 3s to test the effect of such an abrupt change in rupture propagation on the inversion. We consider a smooth slip distribution to test possible occurrence of artificial slip heterogeneity. The synthetics are calculated using crustal model C3 (Figure 2).

6.1. Effect of smoothing

In a first series of inversion tests we consider precise GFs (calculated in the 3D structural model C3) to isolate effects of the chosen smoothing on the inversion. Apart from the target model, Figure 3 shows the inverted slip rates if minor smoothing is considered ($\sigma_D = 1\text{e-}6\text{m}$). The differences between the inverted and the target slip rates are negligible, the precision of the estimated times of peak-slip rate is within plus/minus one time sample. This shows that if the fault parameterization is exactly the same as considered for the target model and if exact GFs are used, only weak regularization is required and an almost perfect source image is obtained. Nevertheless, we emphasize that such smoothing levels are impossible in practice since such ideal conditions are never met. In practical applications the selection of the smoothing strength is to some extent ambiguous. Several ways how to formally determine the suitable smoothing level have been introduced, such as the L-curve method or the ABIC criterion, introduced by Yoshida (1989) in the slip inversion studies.

Here we select three smoothing levels based on the experience from the tests with imprecise GFs and the real-data application to best illustrate the inversion behavior when changing σ_D . The same values of σ_D are used consistently throughout the whole paper. Figure 4 depicts the inversion testing results applying the selected smoothing strengths (larger σ_D means weaker smoothing). Note that we do not show the waveform fits because the seismograms are almost identical in all cases with variance reduction larger than 0.998.

In case of weak smoothing ($\sigma_D = 0.01\text{m}$), slip rates are well resolved over almost the entire fault (see Figure 4). Problematic are artificial secondary slip-rate pulses around the area of delayed rupture. This illustrates that spatial smoothing may generate time-domain artifacts. Indeed, the smoothing constraint is applied to all time instances. Therefore, in the fault region of delayed rupture the slip rates are spatially smeared into neighboring cells at a given time, which introduces spurious peaks in the non-delayed fault area. Conversely, the non-delayed fault area introduces earlier artificial slip-rate peak on the delayed asperity.

When smoothing is increased (Figures 4, b, c), the above-described problem of artificial secondary slip-rate pulses is extended to larger distances away from the border of the delayed asperity. Additionally, the deterioration of the inferred model becomes stronger, especially in the down-dip direction and in the right part of the fault. Figure 4 also shows that with increasing smoothing level there is an apparently stronger temporal smoothing of the slip rates. It results in incorrectly resolved rise-time and rupture time, while still approximately preserving the peak slip-rate times.

The results also suggest that the quality of the inversion decreases with increasing hypocentral distance. Indeed, when increasing the smoothing strength the deterioration of slip rate is weaker closer to the hypocenter (see point no. 3 in Figure 4) than farther from the hypocenter (see point no. 4 in Figure 4). Similar effects can be observed in additional tests that we conducted, based on the SIV “inv1” benchmark (see Appendix and Figure 3A), assuming almost perfect station coverage. A similar observation of decreasing quality of estimated rupture parameters with increasing hypocentral distance was made by Razafindrakoto and Mai (2014). We interpret this behavior as an induced apparent temporal smoothing of slip rates due to the spatial averaging from slip rates on nearby cells. Early in the rupture process, the true slip rates are localized around the hypocenter, while later the slip rates are distributed over a larger portion of the fault. Therefore, the averaging effect is less pronounced in the beginning (near the hypocenter) than later during the rupture.

6.2. Effect of incorrect Green's functions

Here we repeat the above tests, but considering GFs calculated in the approximate 1D structural model (C1) to analyze the impact of using imperfect GFs in the inversion. Figure 5 shows the inversion of the synthetic data when applying identical smoothing as in Figure 4. In case of the smallest σ_D , the inferred model suffers from the presence of many strong artifacts both in the final slip (artificial asperities and low-slip areas) and in the shapes of slip rates (occurrence of artificial multiple peaks). Obviously, the inversion tends to map all the inconsistencies of the GFs into the inferred source model. We point out that if values of σ_D are even smaller than those considered in Figure 5, the slip image becomes much more “noisy” with clearly unphysical rupture propagation (rupture ‘jumping’ from one side of the fault to the other).

Increasing the smoothing leads to suppression of the majority of artificial slip-rate peaks. Thus, smoothing masks effects of using imperfect Green's functions, at the expense of revealing other negative effects of the smoothing. For example, the artificial two peaks of slip-rates in the rupture-delay transition area coincide with those already observed in Figure 4 in case of perfect (3D) GFs, i.e. those arising from the spatial smoothing. Similar interpretation applies to the apparent decrease of slip amplitudes in the bottom and the top-right part of the fault (compare Figures 4 and 5). However, there are additional spurious slip rate multiples, e.g., in the top left and right part of the fault, which were not observed in the case of the perfect 3D GFs. Thus, we associate them with strong disagreement between the 1D and 3D GFs.

Figure 6 shows a comparison of target waveforms with those corresponding to smoothing parameter $\sigma_D = 0.1\text{m}$. Although the variance reduction is 0.99, we do observe significant differences between the waveforms, especially at larger distances (stations MTR, ANT, FMG, CLN). We recall that if the same smoothing is applied when using perfect 3D GFs, the waveform comparison is almost perfect. Thus, differences in target and inverted waveforms in Figure 6 are related to 3D crustal structure complexity that is not captured by the 1D GFs.

Similar to the case of smoothing with perfect 3D GFs, we find that when using approximate 1D GFs the smoothing effect generates an apparent broadening of the slip rates functions (Figure 5). Figure 7 compares inverted peak slip-rate times for identical smoothing ($\sigma_D = 0.1\text{m}$), documenting that the peak slip-rate times are well resolved in both cases of precise and imprecise GFs almost everywhere along the fault. The only exceptions are located at the rupture-delay transition, especially where the artificial slip-rate peaks exceed the true ones. Note that the other inversion example based on the SIV1 benchmark with sharper slip-rate onset shows more significant bias due to smoothing.

6.3. Spike-resolution analysis with imprecise Green's functions

Here we introduce another resolution test. The target source model consists of just a single slip-rate spike located at a prescribed position on the fault. Inversion of such a source model serves to reveal the resolution power of the inversion, which is largely controlled by the effect of smoothing. Furthermore, to capture potential additional consequences when using imprecise GFs, we calculate the target synthetics using GFs from model C3, while we invert the resulting synthetics using the 1D GFs from model C1.

Figure 8 shows examples of our spike-resolution analysis for smoothing $\sigma_D = 0.05\text{m}$ assuming three different positions of the spike on the fault. The inferred slip rates are generally spread in space, documenting the expected effect of smoothing. In fact, the spreading is present even if the same GFs are used for generating target waveforms and their inversion, and is controlled by the value of σ_D . Using different GFs in the forward and inverse calculations introduces additional spurious slip-rate pulses on the fault, whose occurrence and position depend on the position of the tested slip-rate spike. For example, if the spike is located as shown in the middle panel in Figure 8, artificial slip at the shallow right part of the fault can be observed. On the contrary, if the spike is located just 3km further to the right, no slip is inferred at shallow depths but the slip amplitude is larger. We explain this effect by the proximity of the CADO station to the tested location of slip-rate spike. This suggests that the resolution and reliability (e.g., as small artifacts as possible) of the inversion strongly depends on the relative location of the stations with respect to regions of high-moment release and the presence of significant crustal inhomogeneities.

The spike-resolution analysis also allows for testing effects of the station distribution, and may help in defining the station weights prior to the real-data inversion. We have tested cases (not shown here) when a single station was given a much larger weight (i.e. a single station was used in the inversion). In this case, the inverted source model showed forced rupture propagating towards the station, as described first by Olson and Anderson (1988) (see also Zahradník and Gallovič, 2010; Gallovič and Zahradník, 2011). Therefore, good azimuthal station coverage is crucial. If an azimuthal gap exists (which will be the case in almost all real applications), it should be compensated by proper weighting. Stations weights should therefore not be chosen merely according to the measured amplitudes, but also according to spatial density and distribution of the stations. In contrast, increasing the weight of distant stations is advisable to compensate for the geometrical spreading of wave amplitudes, which implicitly decreases the amplitude-based weight of the station. However, the increased weighting of distant stations should be treated with caution due to the general deterioration of quality of (synthetic) GFs with increasing distance that hence may lead to amplification of artifacts due to the imperfection of the GFs.

7. Inversion of real data

In this section we apply the inversion method to the recorded data of the L'Aquila earthquake. Note that the inversion setup for this real-data case is the same as for the above synthetic tests (see description in Section 5).

7.1. Inverted slip models

Figure 9 shows results of real data inversion for various smoothing strengths (σ_D) using 3D GFs for crustal model C2. Values of σ_D are identical to those chosen in the synthetic tests. Also the apparent increase of source complexity with decreasing σ_D is similar to that observed in synthetic tests with imprecise Green's functions (see Figure 5). In particular, the source model obtained with $\sigma_D = 0.01\text{m}$ (top panels in Figure 9) demonstrates how the inversion maps unaccounted wave-propagation effects into the source model.

The other two models, considering $\sigma_D = 0.05\text{m}$ and 0.10m (middle and bottom rows in Figure 9, respectively), are smoother than the previous one. The static slip distribution is dominated by a single slip patch located $\sim 5\text{km}$ above the hypocenter and $\sim 5\text{km}$ to the south-east. This solution resembles slip models inferred in previous studies employing geodetic data (GPS, SAR; e.g., Cheloni et al., 2010; Trasatti et al., 2011; Serpelloni et al., 2012; D'Agostino et al., 2012; Gualandi et al., 2014). Solutions obtained when considering strong motion data (using velocity seismograms) tend to have this large-slip asperity at greater depths (see comparison study performed by Cirella et al., 2012). In addition, Figure 9 shows the distribution of the peak slip-rate times. In all cases, the peak slip-rate times suggest fast up-dip propagation, followed by a delayed along strike propagation, which is also in agreement with other studies.

To gain more insight into the inversion result, Figure 10a shows the rupture evolution in terms of slip-rate snapshots. For reference, we display the hypocenter location (which is not a priori constrained in our inversion scheme) and areas of significant afterslip (Gualandi et al., 2014). We find that the major slip starts $\sim 2\text{-}3\text{s}$ after the origin and $\sim 2\text{km}$ up-dip from the hypocenter. This point corresponds to the origin of the impulsive phase determined by Di Stefano et al. (2011) from the observed seismograms, marking the beginning of the large moment release. The rupture propagates first in the up-dip direction, reaching the surface after 4-5 sec, and then continuing into the region above the afterslip area. About 1-2s later, the rupture appears to re-nucleate at the border of the afterslip area. After perhaps joining the rupture propagating from above, the deeper asperity then starts breaking, avoiding entering the afterslip area to the right.

Figure 10b shows the waveform fit for the model with smoothing parameter $\sigma_D = 0.05\text{m}$, resulting in a total variance reduction of 0.95. Note that due to the chosen station weights (see section Inversion model setup) the quality of the misfit decreases only slightly with increasing distance, although the amplitudes of the distant stations are up to an order of magnitude smaller than those of the near stations. Note that the waveform fit is somewhat worse than in the synthetic case where we used 1D GFs to invert target seismograms computed with the most complex 3D GFs. This suggests that the true Earth structure generates reverberations (mostly at later times) that are not modeled by the structural model by Di Stefano et al. (2011), resulting also in generally lower variance reduction. We speculate that a more accurate velocity model, including the L'Aquila basin, could improve the waveform fit.

7.2. Critical appraisal of details of the inverted model

The synthetic tests presented in Section 6 and in the Appendix warn against taking the inversion result at face value. The inversion, due to the use of imperfect GFs and applying a smoothing constraint, suffers from various artifacts that may mislead the interpreter. Thus, we here critically discuss some detailed features of the source model based on the lessons learned from the synthetic tests, and then present alternative source models whose predicted seismograms, if inverted, would lead to practically the same slip image. Some of our comments are graphically presented in the plot of peak slip-rate times in Figure 9.

Figure 9 shows that the inverted slip rate functions are characterized by two apparent peaks at the hypocenter. Such a shape of the slip-rate function is expected in case of super-shear rupture, in which the first rupture pulse is followed by the trailing Rayleigh pulse (Dunham and Archuleta, 2004; Mello et al., 2014). This mechanism is particularly appealing since the rupture propagated up-dip in in-plane mode at high velocity. However, one has to recall the artifacts introduced by smoothing close to a delayed asperity, suggesting that this particular shape of the slip-rate functions is an artifact rather than a real feature. Cirella et al. (2012) also concluded that there is no signature of supershear rupture at the initial stage of the rupture.

Our inferred model consists of relatively long duration rupture at the large-slip asperity (crack-like rupture behavior). This conflicts with the model by Cirella et al. (2012), who used a nonlinear approach and inferred rather slow but complex rupture propagation, suggesting asperity breakage with highly variable rupture velocity. Since both our and the Cirella models fit data well, this disagreement represents perhaps the ‘true’ uncertainty of the slip inversion. Indeed, if the slow (and complex) propagation of the rupture is correct, the smoothing constraint (see discussion in Section 6), would most likely smear out the inferred slip rates, thereby generating an apparently long duration (i.e. long rise time). Alternatively, one could argue that the result by Cirella et al. (2012) may be affected due to using constraints on the prescribed shape of the slip rate, and prescribed limits on the rupture velocity, rise time, etc. In particular, they limit rise time values to the range 0.75 - 3s, finding a best value ~2.5s, while our inverted model suggests rise time as long as ~5s. Interestingly, Cirella et al. (2012) inferred rather small rise-time uncertainty (variance coefficient of ~0.2). However, small variances are not necessarily a reliable indicator for correct result. Indeed, based on synthetic tests, Razafindrakoto and Mai (2014) and Monelli and Mai (2008) show that in nonlinear slip inversions the true parameter values can lie at the tail of the posterior distribution, ascribing this effect to imperfect shape of the prescribed slip rate function.

Our inferred source models exhibit other areas with multiple slip-rate peaks, especially at the shallow part of the fault. We point out that not only the first or secondary peak may not be real, but that even all of the peaks might be artifacts. Indeed, as a consequence of an inadequate crustal structure, the artificial occurrence of slip-rate peaks at shallow depths is observed in the spike-resolution analysis (Section 6). In particular, when the tested slip-rate spike is located in the area of maximum slip in the real data inversion (see the middle panel in Figure 8), a significant amount of slip is artificially mapped at the top right part of the fault. Thus, we conclude that the shallow slip is not well constrained in our inversion, but rather may be an artifact due both smoothing and the use of imperfect GFs.

Besides the shallow slip, the aspects of our source inversion discussed above are related to rather minor features in the rupture models. They are basically not “visible” in the snapshots of rupture propagation in Figure 10a. Therefore, we believe that the general style of rupture propagation observed is reliable.

8. Discussion and conclusions

In the present study, we employ a linear approach to slip inversion, a technique that recently regains attention as it allows for very flexible source parameterization. This is especially important if rupture propagation complexities (such as delays, multiple rupturing, rupture-propagation reversals, supershear rupture propagation) are expected. In our inversion method, model parameters are samples of slip rate along the discretized fault, in a time window that spans the entire (assumed) rupture duration.. The least-squares inverse solution is regularized assuming spatial smoothing through an a-priori covariance matrix composed of a k^{-2} covariance function and positivity constraint on slip rate samples. As such, the source description is very general with no constraints on the nucleation point, rupture velocity, or shape of the slip-rate function. However, due to the rather large number of model parameters, the inversion result must be carefully appraised given the general non-uniqueness of finite-fault source inversions, and the possibility of obtaining artifacts and biased solutions (Zahradník and Gallovič, 2010; Gallovič and Zahradník, 2011). Thus, the resolving power of the proposed linear inversion approach is first examined by thorough synthetic testing. To correctly assess the performance of our inversion for the real-data application, we use the same data processing and inversion parameterization (e.g. fault discretization and smoothing) for the testing stage as in the later application to the L'Aquila earthquake. We note that our findings overviewed below are in some cases related to our specific inversion method and cannot be understood as universally valid.

8.1. Lessons learned from the synthetic tests

Our synthetic tests aim to understand effect of 3D crustal inhomogeneities and smoothing on linear slip inversions. Generally, when correct (3D) Green's functions (GFs) are used in the inversion, near-fault recordings have resolution power for almost perfect model estimation (Figure 3). However, this is not the case when less precise (1D) GFs are employed. In this case, smoothing constraint must be utilized to effectively damp the arising artificial small-scale heterogeneities.

To better understand this issue, we have analyzed effects of smoothing constraint and imperfect Green's functions through careful synthetic testing (Sections 6.1 and 6.2, respectively), considering i) a smooth slip model with a prescribed rupture delay on a part of the fault, and ii) a single slip-rate spike localized on the fault plane (Section 6.3). In addition, we have performed the inversion for the heterogeneous source model SIV “inv1” of the Slip Inversion Validation (SIV) initiative (Page et al, 2011), which is based on a spontaneous dynamic simulation with heterogeneous initial stress (see Appendix).

We show that the effects of smoothing are non-trivial. Indeed, the ‘averaging effects’ occur on the true slip rates at each time instance, obtaining something like time-dependent local centroids at each time step. This effect is best visible in Figure A2 (compare the middle and right slip rate snapshots. Consequently, since slip rate at a given position on the fault and at a given time instance is affected by spatially distant points on the fault that are at different stage of slipping, the spatial smoothing is translated to the time domain as apparent temporal smoothing (see slip rates at points 3 and 4 in the bottom right panels in Figures 4). The slip rates are thus broadened in time around their maxima, thus the timing of peak slip-rates is potentially better resolved than the rupture time and rise time (that trade-off with each other). However, the latter effect is even stronger if the true slip-rate functions have strong onsets and/or the local rupture front is highly curved (such as observed in dynamic simulations, see Figure A3). In such case, both rise times and peak slip rate times would become biased.

For the same reason, one can expect stronger artificial slip-rate broadening in case of low rupture velocity in a real case, which would be indistinguishable from the case of true longer rise times. In other words, in case of true pulse-like rupture propagating at low rupture velocity, the smoothing constraint would modify this slip image to apparently slow crack-like rupture. Qualitatively similar trade-offs of rupture speed and rise time have been found by Razafindrakoto and Mai (2014). Similarly, close to a delayed asperity, the inferred slip rates contain artificial slip pulses (see slip rates at points 1 and 2 in the bottom right panels in Figures 4).

The spatial smoothing effect is also strongly controlled by station coverage and station weighting. One way to understand these effects is to examine the extreme case of a single-station inversion. The inferred slip model would have artificially amplified values close to the station location, and the inferred rupture evolution would look as if the rupture propagated towards that station (see also Olson and Anderson, 1988, and Gallovič and Zahradník, 2011). This prompts for azimuthally homogenous station coverage and careful station weighting. Regarding the latter, it is advisable to consider weights dependent on the station distance only. In this case, weights are used to compensate for the smaller amplitudes of far-distant stations due to the geometrical spreading (as considered in our synthetic tests based on the L'Aquila earthquake geometry). However, caution must be exercised because the quality of synthetic GFs generally decreases with increasing distance, which may lead to even stronger artifacts due to the imperfection of the GFs. Proper selection of a weighting scheme can be attained through spike resolution tests (see Section 6.3 and Figure 8). Reporting such test in the publication is a good practice for source-inversion studies.

We have performed tests for which synthetics were calculated using 3D GFs from a model with strong random heterogeneities combined with local tomography model (Di Stefano et al., 2011). The waveforms were then inverted using (approximate) 1D GFs from a crustal model composed of homogeneous layers. The imperfections of the GFs give rise to artificial small-scale source heterogeneities not only in the final slip distribution on the fault, but also in the slip-rate functions in terms of multiple slip rate peaks (see Figure 5). Applied smoothing constraints effectively damp these artifacts in the deeper parts of the fault, but to lesser extent in the shallow part. This confirms findings by Ji et al. (2002) and Piatanesi et al. (2007), who report that especially the near-surface slip estimate is strongly affected by the quality of the structural model.

The above-mentioned problems obscure the estimation of the true rupture propagation since i) the smoothing effect depends on the actual behavior of the rupture, ii) and the real effect of imprecise GFs is not perfectly predictable. Therefore, we stress that inversion results should not be taken at face value, but instead require interpretation by questioning particular model features and seeking alternative models that may result in the same slip image after inverting their seismograms.

8.2. Real data inversion

The lessons learned from the synthetic tests help to understand models inferred from the real data of the 2009 Mw6.3 L'Aquila earthquake. We have applied the inversion approach to real data of the 2009 Mw6.3 L'Aquila earthquake, utilizing 3D GFs that considered tomography model and local topography. This real data application represents an extension of previous work by Gallovič and Zahradník (2012), who considered a maximum frequency of 0.2Hz, whereas in the present application the maximum frequency is set to 0.5Hz. The authors considered a simplistic rupture parameterization by means of rectangular homogenous slip patches and 1D GFs. Using the higher maximum frequency allows us to infer more details of

the rupture propagation. Nevertheless, the lessons learned from the synthetic tests must be taken into account to avoid misinterpretation of the inferred source model.

Our basic interpretation is discussed in Figure 9. The inferred slip model resembles previously published solutions using geodetic data, showing a large-slip asperity south-east of the hypocenter. In agreement with other studies, we find evidence for fast up-dip sub-shear rupture propagation, followed by a delayed propagation along strike. We speculate that the rupture was temporarily inhibited by a deep localized velocity-strengthening patch that then experienced afterslip.

Due to the smoothing effect and potential artifacts because of imprecise GFs, other potentially visible features of rupture complexity cannot be quantified unambiguously. For example, the inferred source model contains significant amount of slip in the top right part of the fault. However, the spike-resolution test has shown that this might be just an artifact due to the presence of significant amount of slip in the deeper part of the fault (Figure 8), as a consequence of improper crustal model. Indeed, D'Agostino et al. (2012) showed using DInSAR data that no or only very small co-seismic slip occurred at shallow depths ($\sim 2\text{--}3\text{ km}$ along the fault dip), while significant shallow postseismic slip has occurred there (Cheloni et al., 2010; Gualandi et al., 2014). To fit near source strong-motion recordings in a broad frequency range (0.5-10Hz), Ameri et al. (2012) required slip to vanish at such depths. Thus, the shallow slip in our inversion is likely an artifact.

Our inverted source model comprises several other detailed features, some of which may be explained by theoretical (dynamic) models. Note that these features are conjectural at present, owing to potential artifacts due to smoothing and imprecise GFs. For example, especially if weak smoothing is applied, the inferred source image contains multiple slip pulses. Such slip-rate multiples can be observed also in dynamic models (e.g., Gabriel et al., 2012; Goto et al., 2012; Huang et al., 2014). However, the reliability of the inverted slip-rate multiples can be hardly proven as they are a common artifact if imperfect GFs are used and/or if the true rupture includes complexities in rupture propagation (such as a time delay). Our experience is that the presence of multiple slip-rate pulses suggests poor resolution at the respective part of the fault, rather than a true slip rate complexity. Another questionable feature of the inverted model is long rise time at the large-slip asperity (ie. crack-like rupture evolution). We point out that it is impossible to discriminate whether this feature is real or a smoothing artifact of true pulse-like rupture propagating at low rupture speed. Given the available data and source-inversion techniques, the precise rupture evolution remains inaccessible.

We believe that dynamic modeling of the L'Aquila earthquake will help to discriminate various proposed rupture-model solutions. This well-studied earthquake is characterized by unique lateral composition of parts of the fault that ruptured co-seismically while other parts had mostly postseismic slip. This different slip behavior can be attributed to variations in rate-and-state frictional properties along the fault, with velocity strengthening and velocity weakening, respectively. Such a composition of fault has been previously observed only on larger scales, such as in subduction zone settings (e.g., Perfettini et al., 2010). The co-existence of these two frictionally distinct zones is mainly theoretically studied in terms of long-term loading, seismic cycle, aftershock triggering, and postseismic effects. Kaneko et al. (2008) analyzed the effect of velocity strengthening zone below the surface on co-seismic (strike-slip) rupture, showing inhibition of static slip and decrease of rupture velocity. However, to the best of our knowledge, effects of laterally inhomogeneous frictional parameters, including a distinct velocity-strengthening zone at depth, has not been studied for normal or thrust faulting earthquakes, thus posing an obvious avenue for future research.

A1. Appendix

A1.1. Target model (SIV "inv 1") and inversion setup

Here we analyze the performance of our linear slip-inversion approach based on a synthetic test developed in the framework of the Source Inversion Validation project (SIV; Mai et al., 2007; Page et al., 2011). The particular model "inv1" considered here has been recently utilized in synthetic tests by Razafindrakoto and Mai (2014) and Fan et al. (2014). The source model is an 80°-dipping right-lateral strike-slip fault of 35x20km size, considered to be known. The target rupture model (SIV "inv1", see <http://equake-rc.info/SIV/> for details) is a result of a spontaneous dynamic rupture simulation, assuming random initial stress distribution. Its scalar seismic moment is $M_0=1.06\times 10^{19}$ Nm. We use all 40 well-distributed stations for which seismic waveforms are available (Figure A1). The seismograms are processed using a Butterworth band-pass causal filter in the same range as in the case of the L'Aquila earthquake, i.e. between 0.05 and 0.5 Hz, and then integrated to displacements. The same processing is applied to Green's functions that are calculated in the same crustal model (homogeneous layers) as the one used to synthesize the target waveforms. The parameters are summarized in Table A1. No station weights are considered.

Figure A2 (middle panels) shows the distribution of static slip and peak slip-rate times, and snapshots of the true rupture propagation. The rupture starts at the largest slip patch at the bottom right of the fault, and then propagates radially with slightly faster velocity along strike (in-plane) than in the up-dip (anti-plane) direction. Figure A3 shows examples of slip rates (dashed grey curve) at three points on the fault (depicted in Figure A2). The target slip rates are characterized by sharp onsets due to the fast stress drop from static to dynamic frictional levels.

The inversions described below are performed on a fault that is discretized with 1x1km large sub-faults. Figure A3 shows the (averaged) target slip rates (solid grey curve). Note that the averaging distorts the fine slip rate function stemming from the dynamic simulation in the following way: the averaged slip rates are broader with smaller maxima, they have delayed onset and peak slip-rate time by ~0.5s with respect to the fine ones.

A1.2. Inversion results

Figure A2 shows inversion result for two values of smoothing for the slip distribution, the peak slip-rate times, as well as snapshots of the rupture propagation. In both cases, the general rupture characteristics are well recovered. In case of less smoothing (left column in Figure A2) both slip and peak slip-rate time distributions are very similar to those of the target model, while the model inverted assuming stronger smoothing has smoother slip distribution and somewhat slower rupture propagation. These characteristics are also visible in Figure A3 that compares inferred slip rates with the target ones. Indeed, when increasing the smoothing, the inverted slip rates tend to be broader, with decreased peak amplitude and increased peak slip-rate times. The effect is similar to averaging the target slip rates spatially (compare the dashed and solid grey lines in Figure A3), however, the effect is amplified due to the smoothing constraint that effectively results in spatial smoothing over larger distances.

The above described discrepancies between the target and the inverted models can be understood when looking at the snapshots of the rupture propagation (Figure A2). Especially for the stronger smoothing, the inverted slip-rate snapshots at each time instant resemble spatially smoothed image of the respective true snapshot. This leads not only to the (expected)

decrease of peak slip rate, but also to the apparent larger values of the peak slip-rate times (see also Figure A3). In addition, there is an apparent elongation in the down-dip direction due to the fact that all stations lay above the fault, which is then also responsible for the vertically elongated slip map (Figure A2 top).

Acknowledgement

Observed waveforms were provided by the Italian Strong Motion Database (ITACA, <http://itaca.mi.ingv.it/>). The displacement waveforms obtained from HR-GPS stations were kindly provided by A. Avallone (Avallone et al, 2011). Map figures were prepared using the Generic Mapping Tools package (<http://www.soest.hawaii.edu/gmt/>). Financial support: Grant Agency of Czech Republic 14-04372S and Charles University project UNCE 204020/2012. This study was supported by the King Abdullah University of Science and Technology (KAUST), and numerical simulations were run on the BlueGene-P "Shaheen" of the KAUST Supercomputing Lab.

References

- Aki, K., and P. G. Richards (2002). *Quantitative Seismology*, Univ. Sci., Sausalito, California.
- Ameri, G., M. Massa, D. Bindi, E. D'Alema, A. Gorini, L. Luzi, S. Marzorati, F. Pacor, R. Paolucci, R. Puglia, and Ch. Smerzini (2009). The 6 April 2009, Mw 6.3, L'Aquila (central Italy) earthquake: Strong-motion observations, *Seismol. Res. Lett.*, 80, 951–966.
- Ameri, G., F. Gallovič, and F. Pacor (2012). Complexity of the Mw6.3 2009 L'Aquila (Central Italy) earthquake: 2. Broadband strong-motion modeling, *J. Geophys. Res.*, 117, B04308, doi: 10.1029/2011JB008729.
- Andrews, D. J. (1980). A stochastic fault model: 1. Static case, *J. Geophys. Res.* 85, 3867–3877.
- Avallone, A., M. Marzario, A. Cirella, A. Piatanesi, A. Rovelli, C. Di Alessandro, E. D'Anastasio, N. D'Agostino, R. Giuliani, and M. Mattone (2011), Very high rate (10 Hz) GPS seismology for moderate-magnitude earthquakes: The case of the Mw 6.3 L'Aquila (central Italy) event, *J. Geophys. Res.*, 116(B2), B02305, doi:10.1029/2010JB007834.
- Avallone, A., Rovelli, A., Di Giulio, G., Improta, L., Ben-Zion, Y., Milana, G., and F. Cara (2014). Waveguide effects in very high rate GPS record of the 6 April 2009, Mw 6.1 L'Aquila, central Italy earthquake, *J. Geophys. Res.* 119, 490–501.
- Beresnev, I. A. (2003). Uncertainties in Finite-Fault Slip Inversions: To What Extent to Believe? (A Critical Review), *Bull. Seismol. Soc. Am.* 93, 2445–2458.
- Bernauer, B., A. Fichtner, and H. Igel (2014). Reducing non-uniqueness in finite source inversion using rotational ground motions, *J. Geophys. Res.* 119, 4860–4875.
- Bindi, D., and A. Caponnetto (2001), Tomographic imaging of the earthquake source: numerical validation in two-dimensional approximation, *J. Geophys. Res.*, 106(2000), 6643–6656.
- Cirella, A., A. Piatanesi, M. Cocco, E. Tinti, L. Scognamiglio, A. Michelini, A. Lomax, and E. Boschi (2009). Rupture history of the 2009 L'Aquila (Italy) earthquake from non-

linear joint inversion of strong motion and GPS data, *Geophys. Res. Lett.* 36, L19304, doi:10.1029/2009GL039795.

Cirella, A., A. Piatanesi, E. Tinti, M. Chini, and M. Cocco (2012). Complexity of the rupture process during the 2009 L'Aquila, Italy, earthquake, *Geophys. J. Int.* 190, 607-621.

Clévéde, E., M.-P. Bouin, B. Bukchin, A. Mostinskiy, and G. Patau (2004). New constraints on the rupture process of the 1999 August 17 Izmit earthquake deduced from estimates of stress glut rate moments, *Geophys. J. Int.* 159, 931-942.

Cohee, B. P., and G. C. Beroza (1994). A comparison of two methods for earthquake source inversion using strong motion seismograms, *Ann. Geophys.*, XXXVII, 1515-1538.

D'Agostino, N., D. Cheloni, G. Fornaro, R. Giuliani, and D. Reale (2012). Space-time distribution of afterslip following the 2009 L'Aquila earthquake, *J. Geophys. Res.* 117, B02402, doi:10.1029/2011JB008523.

Das, S., and B. V. Kostrov (1994). Diversity of solutions of the problem of earthquake faulting inversion; application to SH waves for the great 1989 Macquarie Ridge earthquake, *Phys. Earth Planet. Inter.*, 85, 293-318.

Delouis, B., D. Giardini, P. Lundgren, and J. Salichon (2002). Joint Inversion of InSAR, GPS, Teleseismic, and Strong-Motion Data for the Spatial and Temporal Distribution of Earthquake Slip: Application to the 1999 İzmit Mainshock, *Bull. Seism. Soc. Am.* 92, 278-299.

Di Stefano, R., C. Chiarabba, L. Chiaraluce, M. Cocco, P. De Gori, D. Piccinini, and L. Valoroso (2011). Fault zone properties affecting the rupture evolution of the 2009 (Mw 6.1) L'Aquila earthquake (central Italy): insights from seismic tomography, *Geophys. Res. Lett.* 38, L10310.

Dunham, E. M., and R. J. Archuleta (2004). Evidence for a Supershear Transient during the 2002 Denali Fault Earthquake, *Bull. Seismol. Soc. Am.*, 94(6), 256-268.

Fan, W., P. M. Shearer, and P. Gerstoft (2014). Kinematic earthquake rupture inversion in the frequency domain, *Geophys. J. Int.* 199, 1138-1160.

Frankel, A., and L. Wennerberg (1989). Rupture process of the Ms 6.6 Superstition Hills, California, earthquake determined from strong-motion recordings: application of tomographic source inversion. *Bull. Seism. Soc. Am.* 79, 515-541.

Gabriel, A.A., J.-P. Ampuero, L.A. Dalguer, and P.M.Mai (2012). The transition of dynamic rupture modes in elastic media, *J. Geophys. Res.*, Vol. 117, B09311, doi:10.1029/2012JB009468, 2012

Gallovič, F., and J. Zahradník (2011). Toward understanding slip-inversion uncertainty and artifacts II: singular value analysis, *J. Geophys. Res.*, 116, B02309.

Gallovič, F., and J. Zahradník (2012). Complexity of the M6.3 2009 L'Aquila (central Italy) earthquake: 1. Multiple finite-extent source inversion, *J. Geophys. Res.* 117, B04307.

Gallovič, F., J. Zahradník, D. Křížová, V. Plicka, E. Sokos, A. Serpetsidaki, and G.-A. Tselentis (2009). From earthquake centroid to spatial-temporal rupture evolution: Mw 6.3 Movri Mountain earthquake, June 8, 2008, Greece, *Geophys. Res. Lett.* 36, L21310, doi:10.1029/2009GL040283.

Goto, H., Yamamoto, Y., and S. Kita (2012). Dynamic rupture simulation of the 2011 off the Pacific coast of Tohoku Earthquake: Multi-event generation within dozens of seconds, *Earth Planets Space*, Vol. 64 (No. 12), 1167-1175, doi:10.5047/eps.2012.06.002.

Graves, R., and D. Wald (2001). Resolution analysis of finite fault source inversion using one- and three-dimensional Green's functions. I- Strong motions, *J. Geophys. Res.* 106, 8745-8766.

- Gualandi, A., E. Serpelloni, and M. E. Belardinelli (2014). Space-time evolution of crustal deformation related to the Mw 6.3, 2009 L'Aquila earthquake (central Italy) from principal component analysis inversion of GPS position time-series, *Geophys. J. Int.* 197, 174-191.
- Hartzell, S. H., S. Harmsen, and A. Frankel (2010). Effects of 3D Random Correlated Velocity Perturbations on Predicted Ground Motions, *Bull. Seismol. Soc. Am.* 100, 1415-1426.
- Hartzell, S. H., and T. H. Heaton (1983). Inversion of strong ground motion and teleseismic waveform data for the fault rupture history of the 1979 Imperial Valley, California, earthquake, *Bull. Seismol. Soc. Am.* 73, 1553-1583.
- Hartzell, S. and P. Lui (1995). Determination of earthquake source parameters using a hybrid global search algorithm, *Bull. Seis. Soc. Am.* 85, 616-524.
- Hartzell, S., P. Lui, and C. Mendoza (1996). The 1994 Northridge, California, earthquake: Investigation of rupture velocity, risetime and high-frequency radiation, *J. Geophys. Res.* 101, B9, 20091-20108.
- Herrero, A. and P. Bernard (1994). A kinematic self-similar rupture process for earthquakes, *Bull. Seism. Soc. Am.* 84, 1216-1228.
- Huang, Y., J.-P. Ampuero, and D. V. Helmberger (2014). Earthquake ruptures modulated by waves in damaged fault zones, *J. Geophys. Res.* 119, 3133-3154.
- Cheloni, D., N. D'Agostino, E. D'Anastasio, A. Avallone, S. Mantenuto, R. Giuliani, M. Mattone, S. Calcaterra, P. Gambino, D. Dominici, F. Radicioni, and G. Fastellini (2010). Coseismic and initial post-seismic slip of the 2009 M w 6.3 L'Aquila earthquake, Italy, from GPS measurements, *Geophys. J. Int.* 181, 1539-1546.
- Imperator, W., and M. P. Mai (2012). Broad-band near-field ground motion simulations in 3-dimensional scattering media, *Geophys. J. Int.* 192, 725-744.
- Ji, C., D. Wald, and D. V. Helmberger (2002). Source description of the 1999 Hector Mine, California, earthquake, part I: Wavelet domain inversion theory and resolution analysis, *Bull. Seismol. Soc. Am.* 92, 1192-1207.
- Kaneko, Y., N. Lapusta, and J.-P. Ampuero (2008). Spectral element modeling of spontaneous earthquake rupture on rate and state faults: Effect of velocity-strengthening friction at shallow depths, *J. Geophys. Res.*, 113(B9), 1-17, doi:10.1029/2007JB005553.
- Konca, O. A., Y. Kaneko, N. Lapusta, and J.-P. Avouac (2013). Kinematic Inversion of Physically Plausible Earthquake Source Models Obtained from Dynamic Rupture Simulations, *Bull. Seism. Soc. Am.* 103, 2621-2644.
- Lawson, C. L., and R. J. Hanson (1974). *Solving Least Square Problems*, 340 pp., Prentice-Hall, Upper Saddle River, N. J.
- Lee, S. J., Komatitsch, D., Huang, B. S., and Tromp, J. (2009), Effects of topography on seismic-wave propagation: an example from northern Taiwan, *Bull. Seismol. Soc. Am.*, 99(1), 314-325.
- Luo, Y., and R. Duraiswami (2011). Efficient Parallel Nonnegative Least Squares on Multicore Architectures, *SIAM J. Sci. Comput.* 33, 2848-2863.
- Magnoni, F., E. Casarotti, A. Michelini, A. Piersanti, D. Komatitsch, D. Peter, and J. Tromp (2013), Spectral-Element Simulations of Seismic Waves Generated by the 2009 L'Aquila Earthquake, *Bull. Seismol. Soc. Am.* 104, 73-94.
- Mai, P. M., and G. C. Beroza (2002), A spatial random field model to characterize complexity in earthquake slip, *J. Geophys. Res.*, 107(B11), 2308, doi:10.1029/2001JB000588.
- Mai, P. M., J. Burjanek, B. Delouis, G. Festa, C. Holden, D. Monelli, and T. Uchide (2007). Earthquake source inversion blindtest: Initial results and further developments, *Eos Trans. AGU* 88, 855-877.

- Mai, P.M., and K.K.S Thingbaijam (2014). SRCMOD: An online database of finite-fault rupture model, *Seis. Res. Lett.*, Nov/Dec 2014
- Mello, M., H. S. Bhat, A. J. Rosakis, and H. Kanamori (2014). Reproducing the supershear portion of the 2002 Denali earthquake rupture in laboratory, *Earth Planet. Sci. Lett.*, 387, 89–96, doi:10.1016/j.epsl.2013.11.030.
- Menke, W. (1985). Imaging fault slip using teleseismic waveforms: analysis of a typical incomplete tomography problem, *Geophys. J. R. Astron. Soc.* 81, 197–204.
- Monelli, D., and M. P. Mai (2008). Bayesian inference of kinematic earthquake rupture parameters through fitting of strong motion data, *Geophys. J. Int.* 173, 220-232.
- Monelli, D., M. P. Mai, S. Jónsson, and D. Giardini (2009). Bayesian imaging of the 2000 Western Tottori (Japan) earthquake through fitting of strong motion and GPS data, *Geophys. J. Int.* 176, 135-150.
- Nilsson, S., Petersson, A. N., Sjögreen, B., and Kreiss, H. O. (2007), Stable difference approximations for the elastic wave equation in second order formulation, *SIAM J. Numer. Anal.*, 45(2), 1902-1936.
- Olson, A. H., and J. G. Anderson (1988). Implications of frequency-domain inversion of earthquake ground motions for resolving the space-time dependence of slip on an extended fault, *Geophys. J. Int.* 94, 443-455.
- Page, M., P. Mai, and D. Schorlemmer (2011). Testing earthquake source inversion methodologies, *Eos Trans. AGU* 92, 75.
- Perfettini, H., Avouac, J.-P., Tavera, H., Kositsky, A., Nocquet, J.-M., Bondoux, F., Chlieh, M., Sladen, A., Audin, L., Farber, D. L., and Soler, P. (2010). Seismic and aseismic slip on the Central Peru megathrust, *Nature* 465, 78-81.
- Petersson, N. A., and B. Sjögreen (2012). Stable and efficient modeling of anelastic attenuation in seismic wave propagation, *Comm. Comput. Phys.* 12, 193-225.
- Piatanesi, A., A. Cirella, P. Spudich, and M. Cocco (2007). A global search inversion for earthquake kinematic rupture history: Application to the 2000 western Tottori, Japan earthquake, *J. Geophys. Res.* 112, B07314, doi:10.1029/2006JB004821.
- Poiata, N., K. Koketsu, A. Vuan, and H. Miyake (2012). Low-frequency and broad-band source models for the 2009 L'Aquila, Italy, earthquake, *Geophys. J. Int.* 191, 224-242.
- Razafindrakoto, H. N. T., and P. M. Mai (2014). Uncertainty in Earthquake Source Imaging Due to Variations in Source Time Function and Earth Structure, *Bull. Seismol. Soc. Am.*, 104(2), doi:10.1785/0120130195.
- Sekiguchi, H., K. Irikura, and T. Iwata (2000), Fault geometry at the rupture termination of the 1995 Hyogo-ken Nanbu earthquake, *Bull. Seism. Soc. Am.* 90, 117-133.
- Sekiguchi, H., K. Irikura, and T. Iwata (2002). Source inversion for estimating the continuous slip distribution on a fault - introduction of Green's functions convolved with a correction function to give moving dislocation effects in subfaults, *Geophys. J. Int.* 150, 377-391.
- Serpelloni, E. L. Anderlini, and M. E. Belardinelli (2012). Fault geometry, coseismic-slip distribution and Coulomb stress change associated with the 2009 April 6, Mw 6.3, L'Aquila earthquake from inversion of GPS displacements, *Geophys. J. Int.* 188, 473-489.
- Shao, G., and C. Ji (2012). What the exercise of the SPICE source inversion validation BlindTest 1 did not tell you, *Geophys. J. Int.* 189, 569-590.
- Somerville, P., K. Irikura, R. Graves, S. Sawada, D. Wald, N. Abrahamson, Y. Iwasaki, T. Kagawa, N. Smith, and A. Kowada (1999). Characterizing crustal earthquake slip models for the prediction of strong ground motion, *Seismol. Res. Lett.* 70, 59-80.

Spudich, P., and R. J. Archuleta (1987). Techniques for earthquake ground motion calculation with applications to source parameterization of finite faults, in *Seismic Strong Motion Synthetics*, edited by B. A. Bolt, pp. 205– 265, Academic, San Diego, Calif.

Takemura, S., and Furumura, T. (2013), Scattering of high-frequency P wavefield derived by dense Hi-net array observations in Japan and computer simulations of seismic wave propagations, *Geophys. J. Int.*, 193, 421-436.

Tinti, E., Scognamiglio, L., Cirella, A., and M. Cocco (2014). Up-dip directivity in near-source during the 2009 L'Aquila main shock, *Geophys. J. Int.* 198, 1618-1631.

Trasatti, E., C. Kyriakopoulos, and M. Chini (2011). Finite element inversion of DInSAR data from the Mw 6.3 L'Aquila earthquake, 2009 (Italy), *Geophys. Res. Lett.* 38, L08306.

Valoroso, L., L. Chiaraluce, D. Piccinini, R. Di Stefano, D. Schaff, and F. Waldhauser (2013). Radiography of a normal fault system by 64,000 high-precision earthquake locations: The 2009 L'Aquila (central Italy) case study, *J. Geophys. Res.* 118, 1156-1176.

Yano, T. E., G. Shao, Q. Liu, Ch. Ji, and R. J. Archuleta (2014). Coseismic and potential early afterslip distribution of the 2009 Mw 6.3 L'Aquila, Italy earthquake, *Geophys. J. Int.* 199, 23-40.

Yoshida, S. (1989). Waveform inversion using ABIC for the rupture process of the 1983 Hindu Kush earthquake, *Phys. Earth Planet. Inter.* 56, 389–405.

Zahradník, J., and F. Gallovič (2010). Toward understanding slip inversion uncertainty and artifacts, *J. Geophys. Res.* 115, B09310, doi:10.1029/2010JB007414.

Zhang, Y., W. Feng, Y. Chen, L. Xu, Z. Li, and D. Forrest (2012). The 2009 L'Aquila Mw6.3 earthquake: a new technique to locate the hypocentre in the joint inversion of earthquake rupture process, *Geophys. J. Int.* 191, 1417-1426.

Table 1 – Model and computational parameters considered in both the synthetic tests and the inversion of the real recordings of the Mw 6.3 2009 L’Aquila earthquake.

Parameters	Values
Fault mechanism	Strike: 140°, dip: 50°, rake: -90°
Fault dimension	Length 20 km, width 15 km
Focal depth	9.0 km
Nucleation point position (from NW fault edge) ¹	Up-dip: 4 km, along strike: 6 km
Nucleation point geographical coordinates ¹	42.339°N, 13.381°E
Scalar seismic moment	2.5×10^{18} Nm
Spatial fault discretization	1 x 1 km
Time sampling	0.4 s
Duration of slip-rate functions	10 s
Waveform frequency range (displacements)	0.00 - 0.5 Hz (GPS stations)
	0.05 – 0.5 Hz (accelerometers)
Station weights	1 (AQG, AQU)
	1/3 (ROIO, CADO)
	3 (others)

¹ The nucleation point position is considered only in the forward models in the synthetic tests. The inverse problem is formulated without the prescription of a nucleation point. The point serves also as a reference point to describe the geographic position of the fault plane position.

Table A1 – Model and computational parameters considered for the SIV “inv1” tests.

Parameters	Values
Fault mechanism	Strike: 90°, dip: 80°, rake: 180°
Fault dimensions	Length 35 km, width 20 km
Focal depth	14.0 km
Nucleation point position (from NW fault edge)	Up-dip: 6 km, along strike: 27 km
Scalar seismic moment	1.06×10^{19} Nm
Spatial fault discretization	1 x 1 km
Time sampling	0.4 s
Duration of slip-rate functions	10 s
Waveform frequency range (displacements)	0.05 – 0.5 Hz
Station weights	Equal for all stations

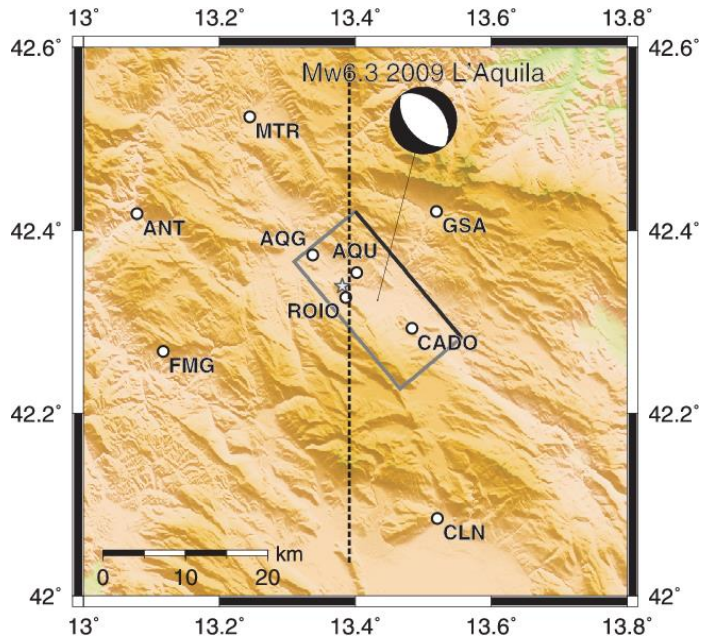


Figure 1: Map view of stations used in this study and fault-plane solution of the L'Aquila mainshock. CADO and ROIO are HR-GPS stations, while the others are accelerometric stations. The rectangle outlines the surface-projection of the fault model considered (fault top side is in black), the star marks the epicenter. The dashed line indicates the location of the velocity cross-sections shown in Figure 2.

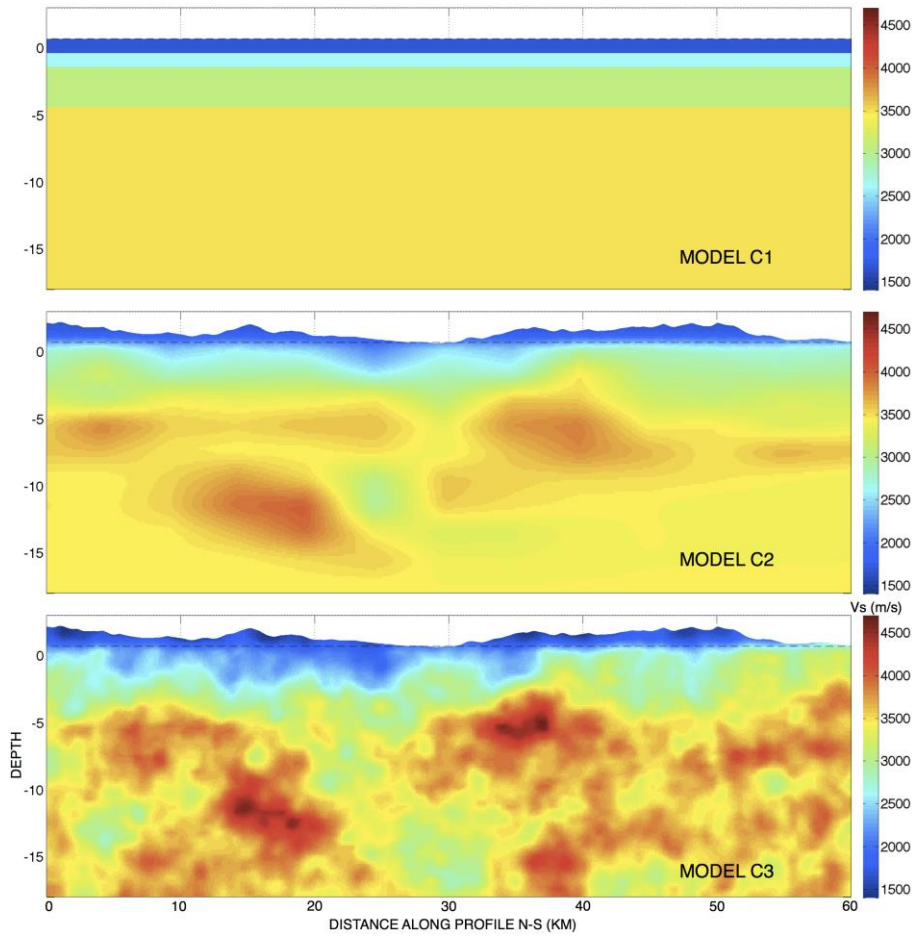


Figure 2: Cross-section of the crustal models for the L'Aquila region considered in this study (see Figure 1). C1: 1D regional velocity model (Ameri et al., 2012). C2: 3D tomographic model of Di Stefano et al. (2011). C3: Model C2 with superposed random velocity perturbations. Velocity heterogeneities follow a Von Karman correlation function (Imperator and Mai, 2013) with correlation length 5km, Hurst exponent 0.3 and standard deviation 10%. Model C3 is used to generate input data for the synthetic tests, which are then inverted using the crustal models C1 and C3. Model C2 is used in the inversion of the real data recorded during the L'Aquila earthquake.

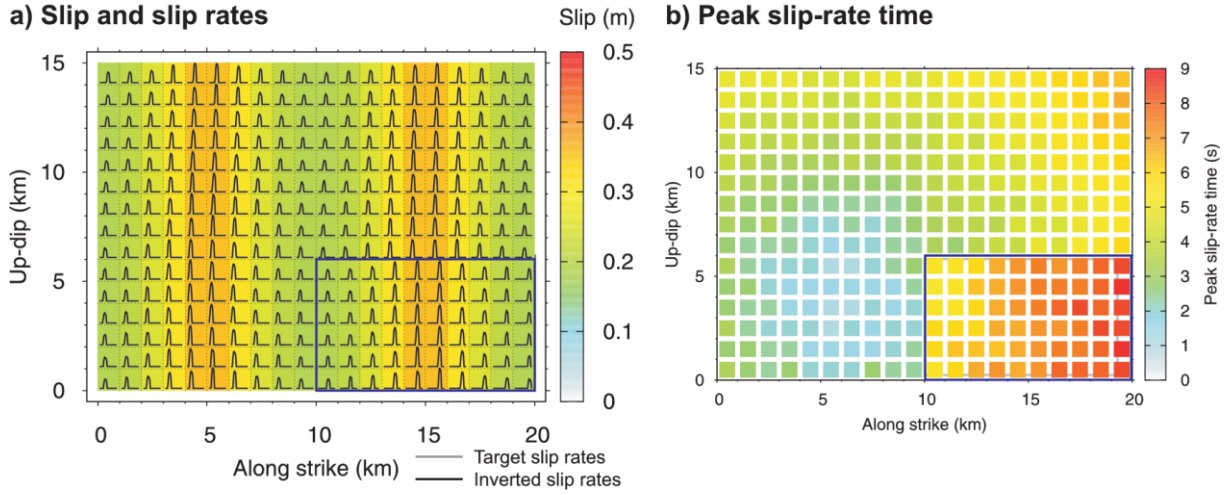


Figure 3: (a) Slip model for benchmarking the inversion approach, including slip-rate functions of 10s duration plotted on each of the 1x1km subfault (black lines). All the slip-rate functions start at the hypocentral time, thus covering the total rupture duration. (b) Rupture times at which the peak slip-rate is achieved. Note the delayed rupture in the bottom right (blue rectangle). Panel (a) shows both the target and inverted slip rates (see legend). The inversion is carried out on displacement waveforms calculated using crustal model C3 (Figure 2), making no prior assumption on the rupture-propagation speed, applying very weak smoothing, and using the Green's functions (GFs) computed also for model C3. The use of exact GFs allows for a very weak regularization (slip rates in black and grey are indistinguishable), leading to an almost perfect source image, with predicted peak-slip rate times within one time sample from the target ones.

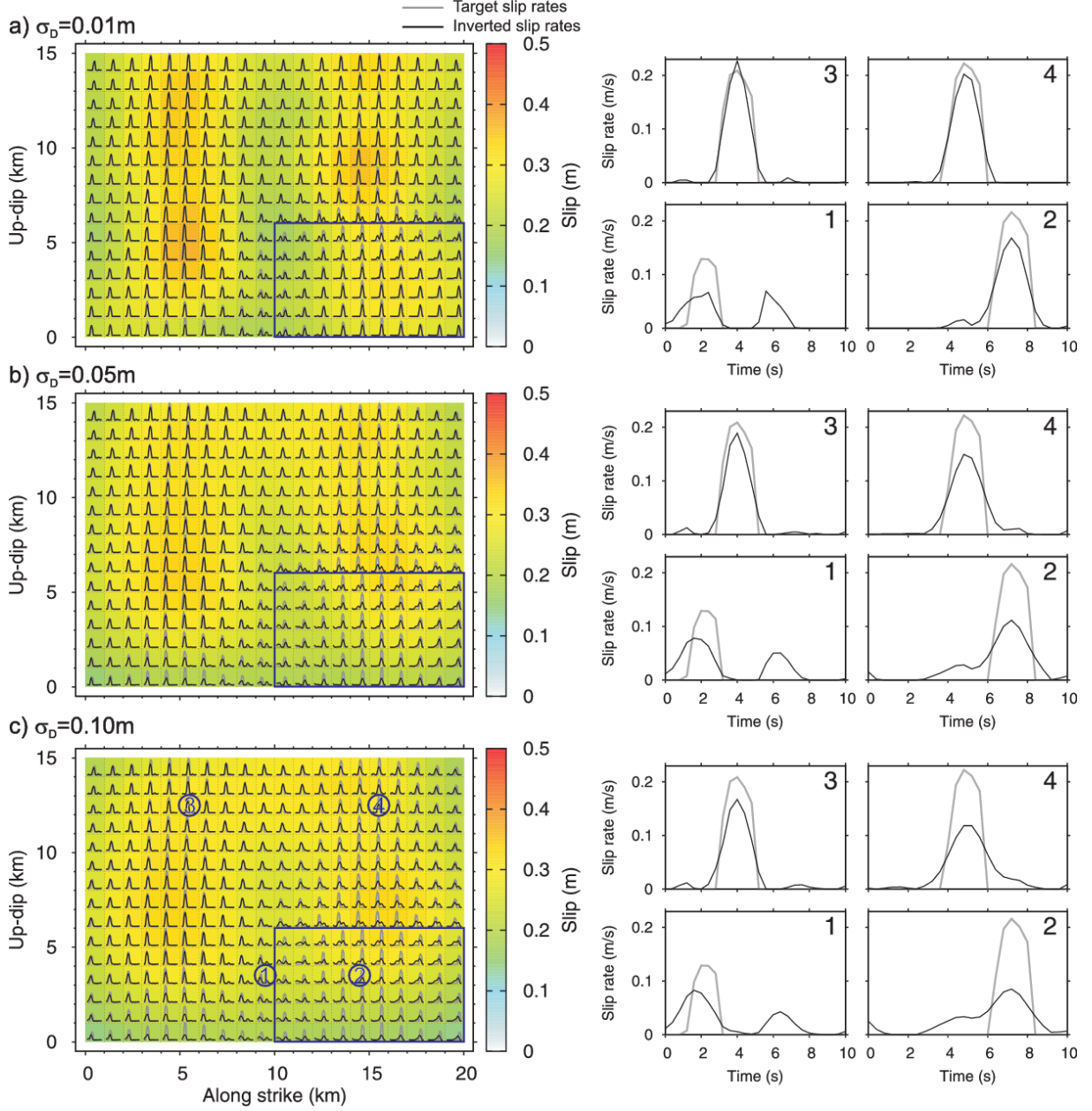


Figure 4: Inversion of the synthetic data with precise 3D Green's functions (crustal model C3 in Figure 2) for various smoothing strengths (the larger σ_D , the weaker the smoothing) to isolate the effect of smoothing. Blue rectangles in the left panels indicate where rupture is delayed in the target model (see also Figure 3). The right panels zoom into slip rates at selected points on the fault (see the bottom left panel for their position). Target slip rates are depicted by grey lines; the inverted ones are shown in black.

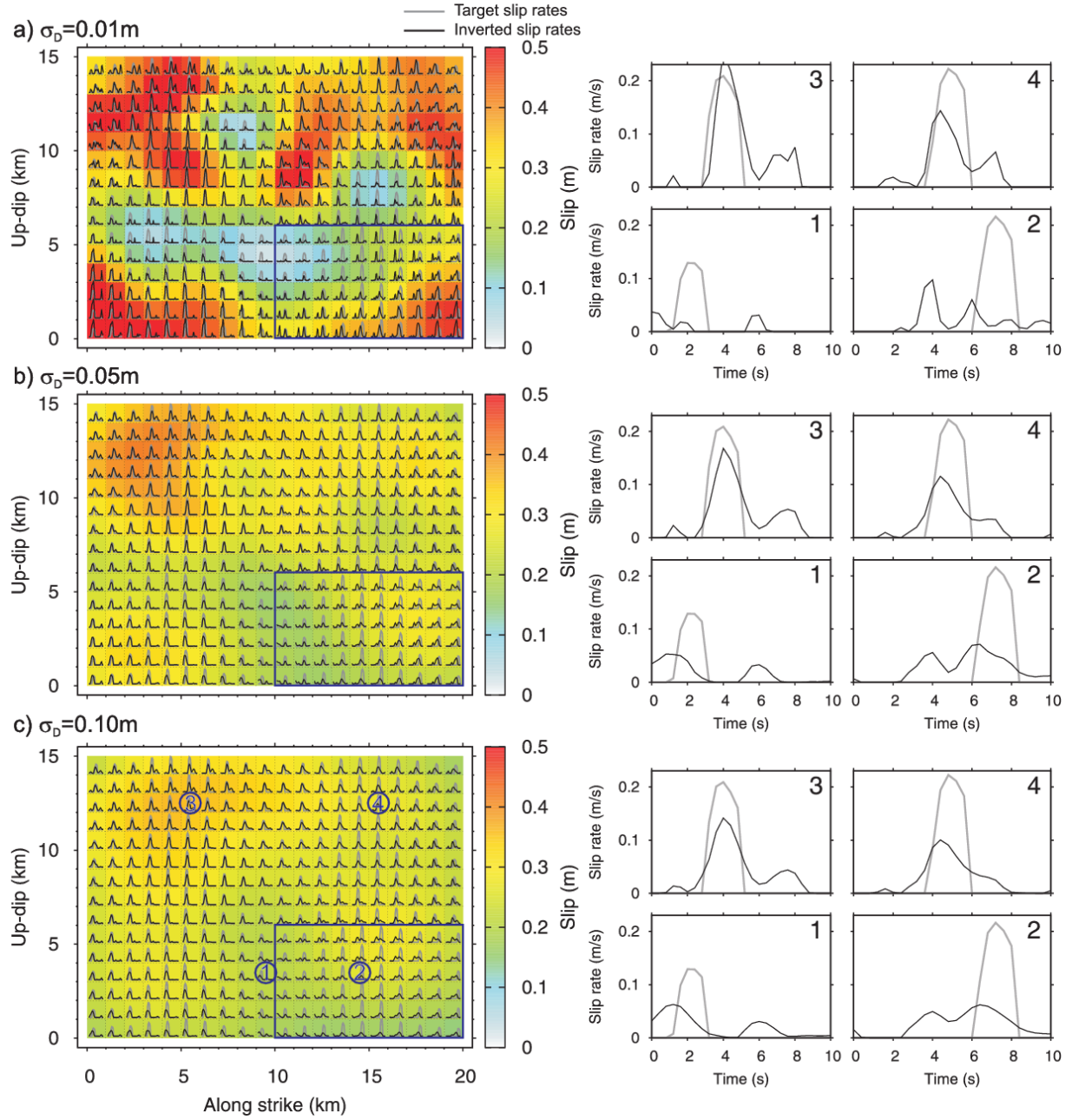


Figure 5: Same as Figure 4 but for the case when approximate (1D) Green's functions (crustal model C1 in Figure 2) are used in the inversion.

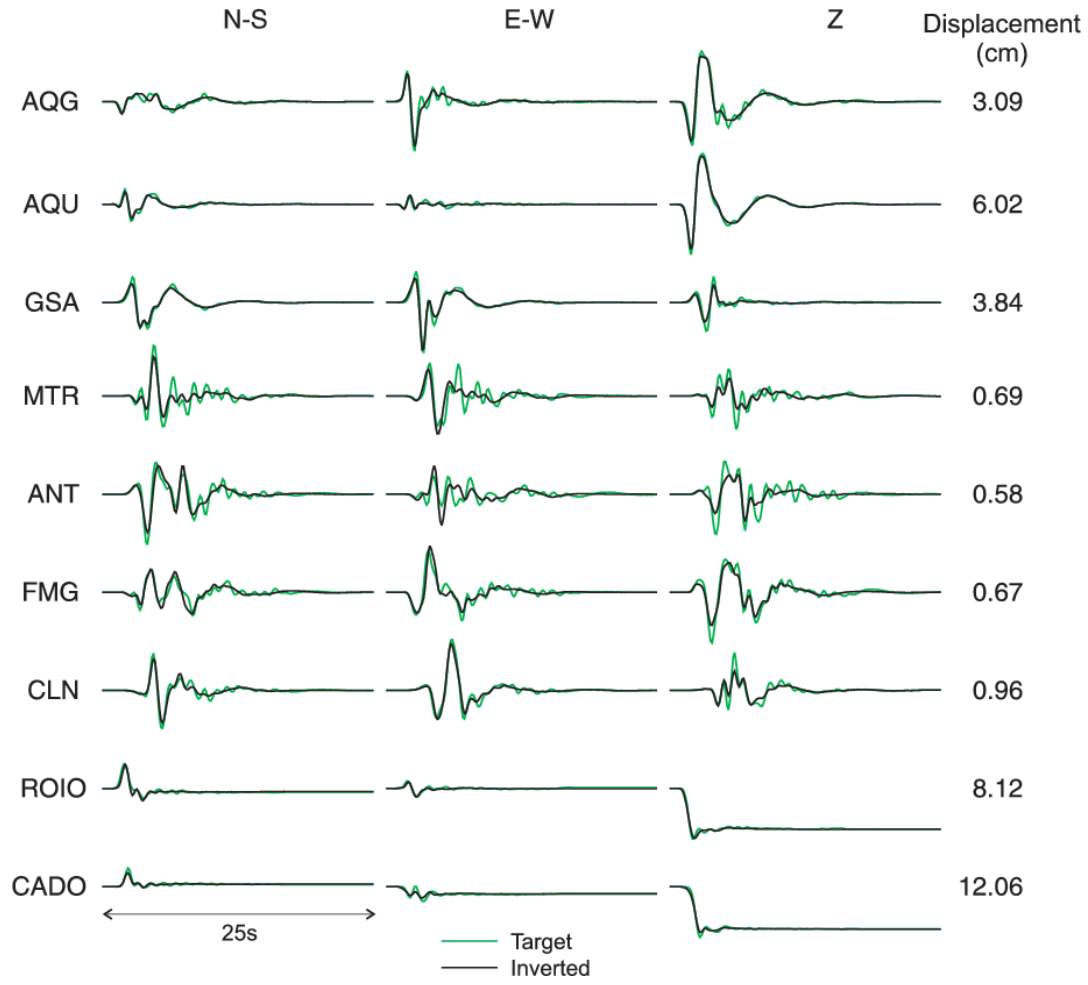
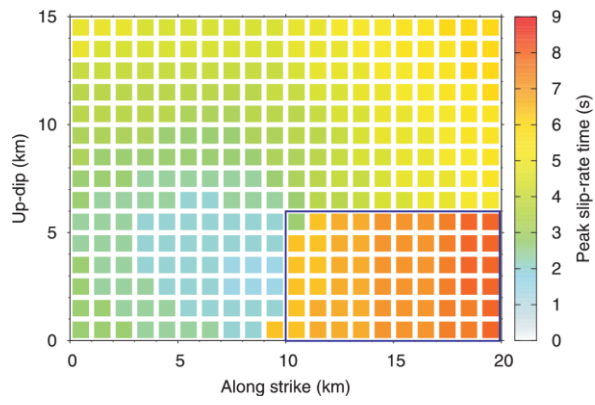


Figure 6: Comparison of target waveforms (green) calculated using the 3D structural model C3 and predicted ones (black) corresponding to the inverted source model using 1D Green's functions (model C1) using smoothing $\sigma_D = 0.1\text{m}$. Variance reduction is 0.99.

a) 3D GF (model C3)



b) 1D GF (model C1)

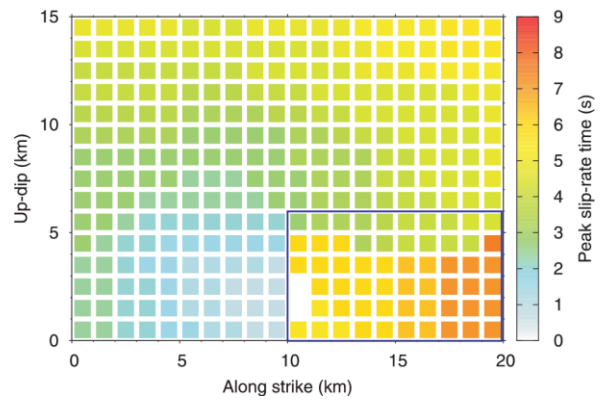


Figure 7: Stability of peak slip-rate times (smoothing $\sigma_D=0.05m$). The delayed rupture area of the target model is marked by the blue rectangle.

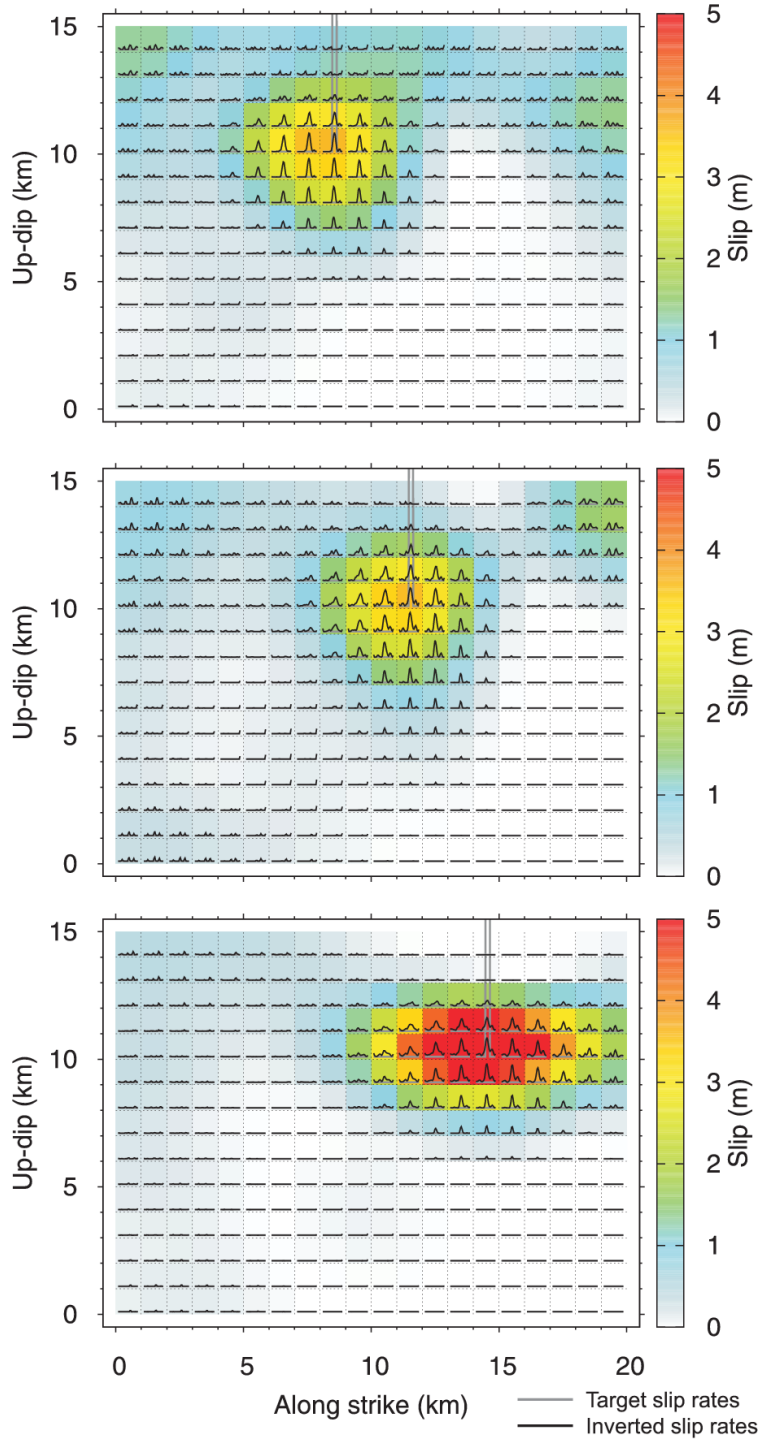


Figure 8: Tests showing inversion results (smoothing $\sigma_D = 0.05\text{m}$) when the target model consists of a single slip-rate spike at a selected point on the fault and when the synthetics are computed in the 3D medium (grey), while the inversion is performed with 1D Green's functions (black). The individual plots correspond to different choices of the position of the target slip-rate spike.

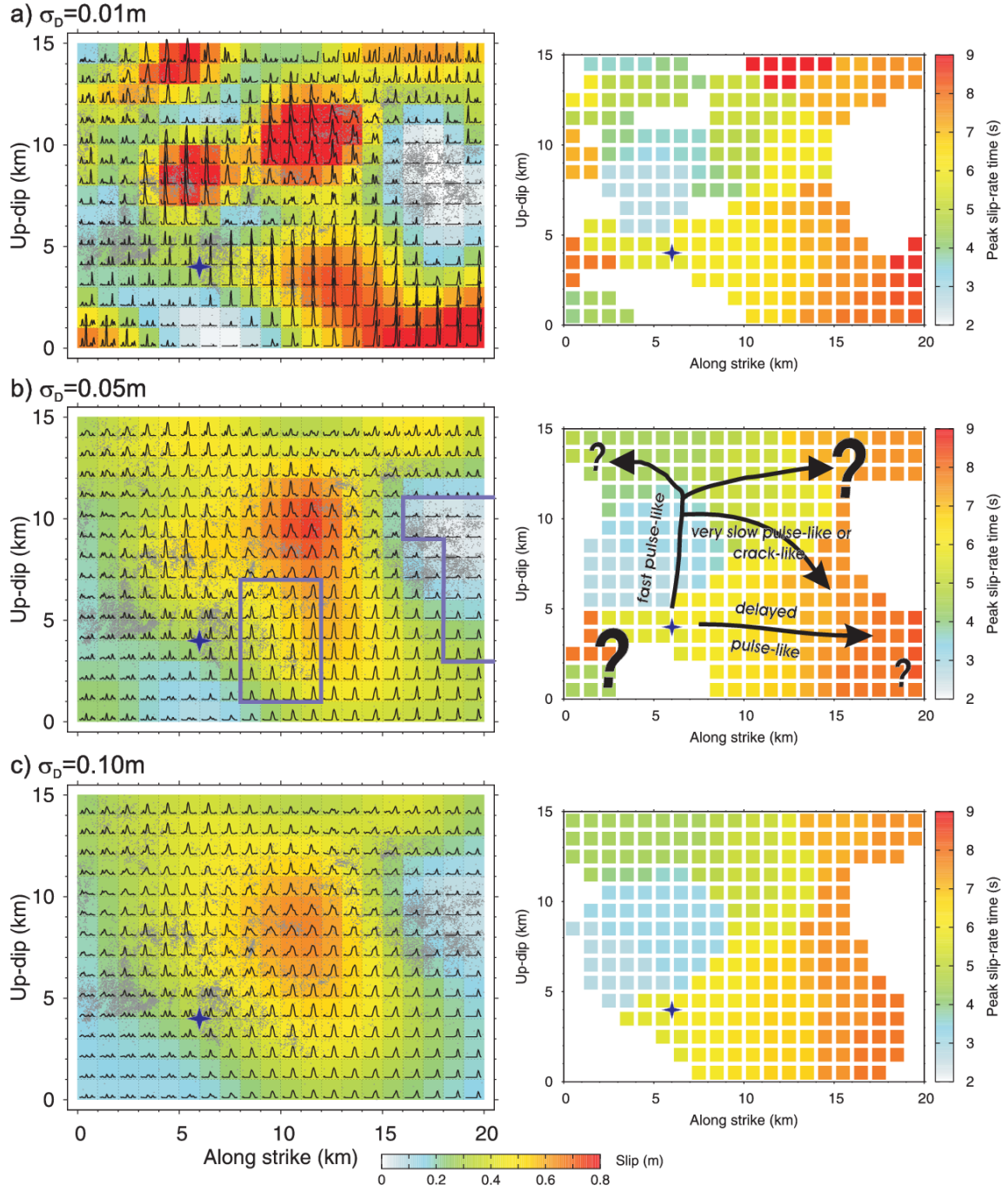


Figure 9: Inversion of the L'Aquila earthquake real dataset using 3D GFs for crustal model C2 and assuming different smoothing strengths (a-c), plotted in terms of slip and slip-rate functions along the fault (left column) and peak slip-rate times (right column). The duration of the slip-rate functions in the left panels is 10s, starting at the hypocentral time, thus covering the total rupture duration. For reference, the star denotes the hypocenter (not used in our inversion approach), small grey dots superimposed on the slip plots represent on-fault aftershocks (within 500m from the fault plane) relocated by Valoroso et al. (2013), and the grey boxes depict major afterslip regions inferred by Gualandi et al. (2014). The arrows and text in the center row in the right column refer to critical interpretation of the inverted model, see text for details.

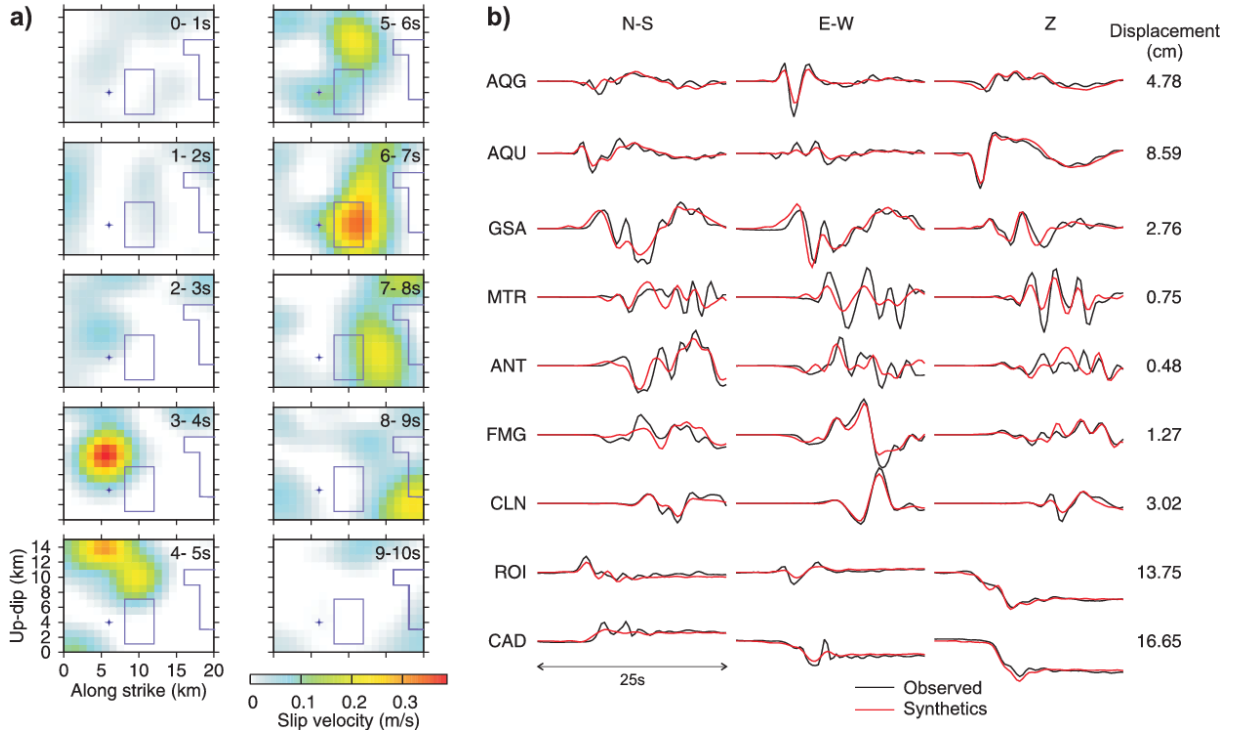


Figure 10: (a) Rupture evolution of the L'Aquila earthquake as revealed from the real data inversion (smoothing $\sigma_D = 0.05\text{m}$ in Figure 9) shown in form of snapshots at 1-sec time intervals. The blue areas depict major afterslip regions by Gualandi et al. (2014) and star denotes the hypocenter (not used in our inversion). (b) Observed (black) and predicted (red) displacement waveform; variance reduction is 0.95.

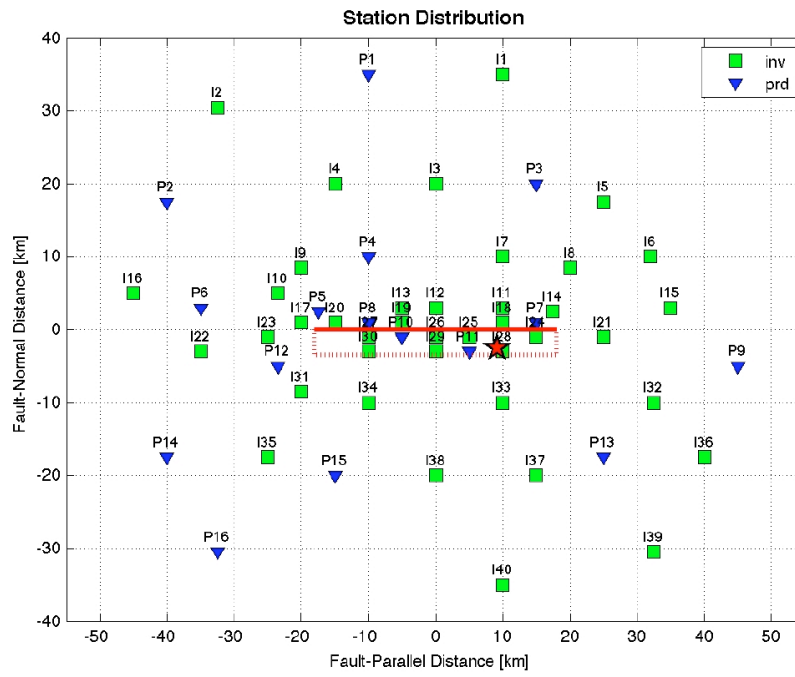


Figure A1: Fault and station geometry of the SIV test “inv1”. See <http://equake-rc.info/SIV/> for details.

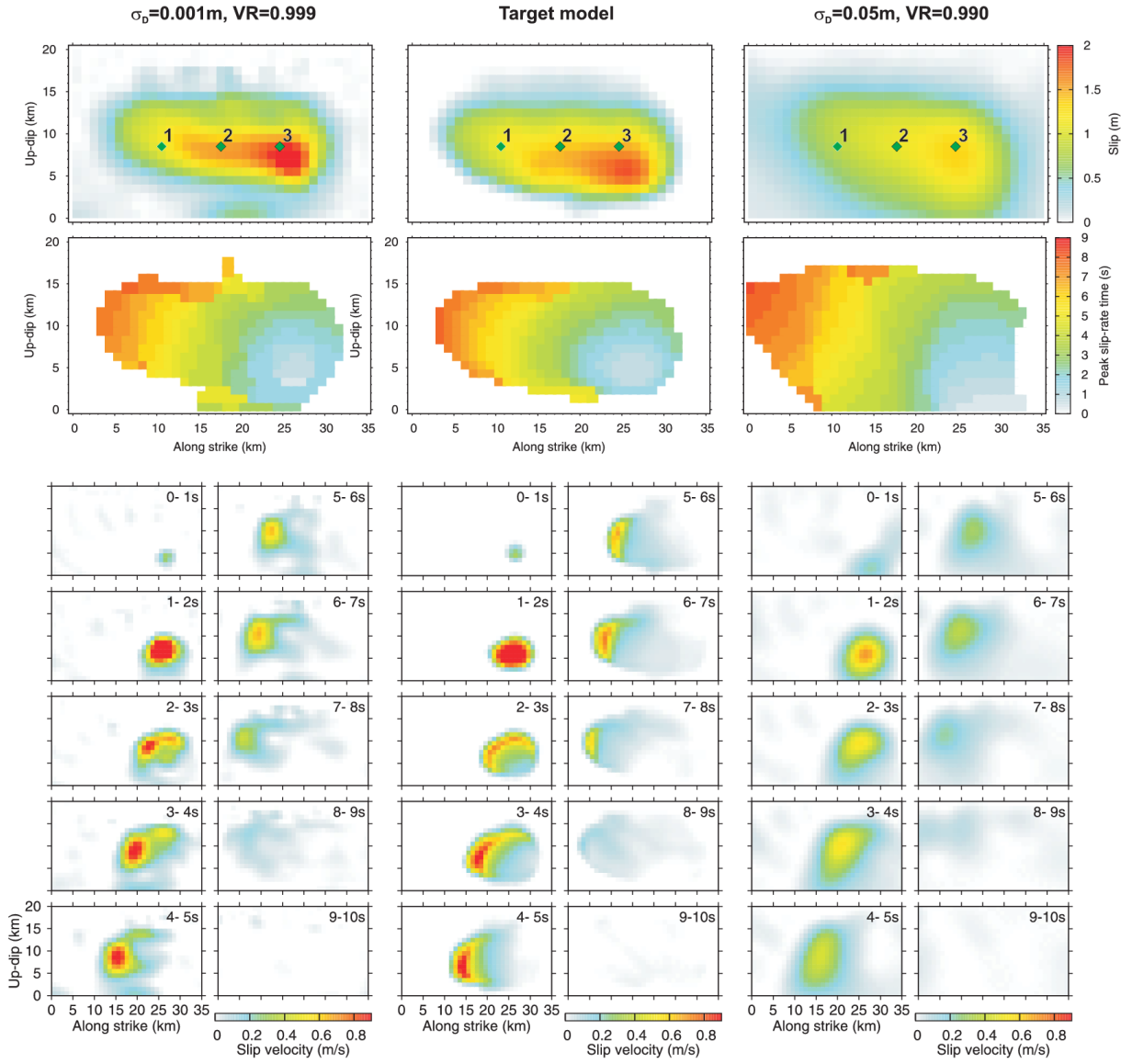


Figure A2: Inversion of the SIV test “inv1” for two values of smoothing (left and right column), compared to the target model (center column). Top row: Final slip. Diamonds denote points, for which the slip rate functions are compared in Figure A3. Middle row: Comparison of peak slip-rate times. Bottom rows: Snapshots (1-sec time interval) of rupture evolution.

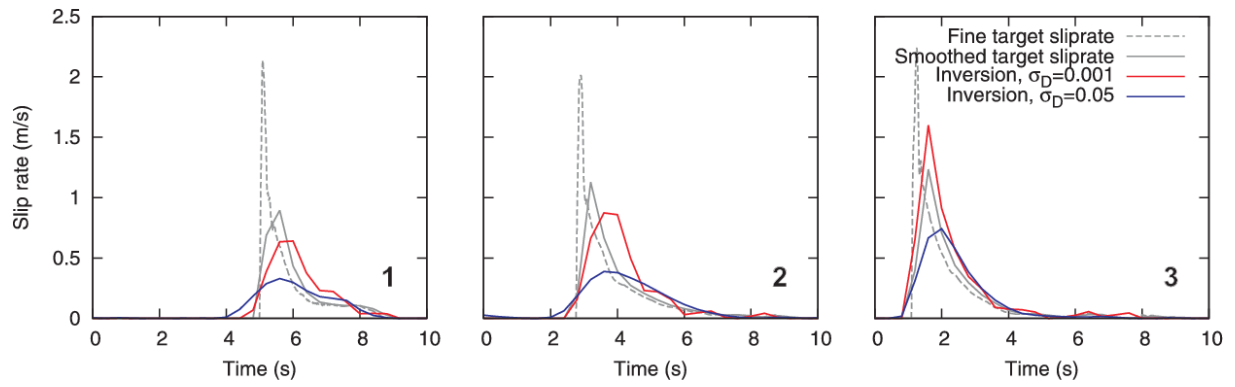


Figure A3: Comparison of slip rates at selected points on the fault (see Figure A2). Grey dashed and solid lines represent slip rates of the finely sampled model (taken directly from the dynamic simulation) and those calculated by averaging over a 1km x 1km subfault, respectively. The number in the bottom right of each panel refers to the slip-rate location on the fault, depicted in Figure A2.